MAHALO Deep Cluster Survey II. Characterizing massive forming galaxies in the Spiderweb protocluster at $z = 2.2$

Rhythm Shimakawa [1]⋆ Yusei Koyama,[1] Huub J. A. Röttgering,[2] Tadayuki Kodama,[3] Masao Hayashi,[4] Nina A. Hatch [5] Helmut Dannerbauer,[6,7] Ichi Tanaka,[1] Ken-ichi Tadaki,[4] Tomoko L. Suzuki,[3] Nao Fukagawa,[8] Zheng Cai[9] and Jaron D. Kurk[10]

[1]*Subaru Telescope, National Astronomical Observatory of Japan, National Institutes of Natural Sciences, 650 North A'ohoku Place, Hilo, HI 96720, USA*
[2]*Leiden Observatory, Leiden University, PO Box 9513, NL-2300 RA Leiden, the Netherlands*
[3]*Astronomical Institute, Tohoku University, Aoba-ku, Sendai 980-8578, Japan*
[4]*National Astronomical Observatory of Japan, Osawa, Mitaka, Tokyo 181-8588, Japan*
[5]*School of Physics and Astronomy, University of Nottingham, University Park, Nottingham NG7 2RD, UK*
[6]*Instituto de Astrofísica de Canarias, E-38205 La Laguna, Tenerife, Spain*
[7]*Universidad de La Laguna Dpto. Astrofísica, E-38206 La Laguna, Tenerife, Spain*
[8]*Department of Astronomical Science, SOKENDAI, Osawa, Mitaka, Tokyo 181-8588, Japan*
[9]*UCO/Lick Observatory, University of California, 1156 High Street, Santa Cruz, CA 95064, USA*
[10]*Max-Planck-Institut für Extraterrestrische Physik, Giessenbachstraße 1, D-85748 Garching, Germany*

ABSTRACT

This paper is the second in a series presenting the results of our deep H α-line survey towards protoclusters at $z > 2$, based on narrow-band imaging with the Subaru Telescope. This work investigates massive galaxies in a protocluster region associated with a radio galaxy (PKS $1138 - 262$), the Spiderweb galaxy, at $z = 2.2$. Our 0.5 mag deeper narrow-band imaging than previous surveys collects a total of 68 H α emitters (HAE). Here, 17 out of the 68 are newly discovered protocluster members. First, a very high characteristic stellar mass of $M_\star^* = 10^{11.73}$ $M_\odot$ is measured from a Schechter function fit to the mass distribution of HAEs. Together with the Chandra X-ray data, we find that four out of six massive HAEs ($M_\star > 10^{11}$ $M_\odot$) show bright X-ray emission, suggesting that they host active galactic nuclei (AGNs). Their mass estimates, therefore, would be affected by the nuclear emission from AGNs. Notably, the X-ray-detected HAEs are likely positioned near the boundary between star-forming and quiescent populations in the rest-frame *UVJ* plane. Moreover, our deep narrow-band data succeed in probing the bright H α (+ [N II]) line nebula of the Spiderweb galaxy extending over $\sim$100 physical kpc. These results suggest that the massive galaxies in the Spiderweb protocluster are on the way to becoming the bright red sequence objects seen in local galaxy clusters, where AGNs might play an essential role in their quenching processes, though a more statistical database is needed to build a general picture.

Key words: galaxies: clusters: individual: PKS 1138-262 – galaxies: evolution – galaxies: formation – galaxies: high-redshift.

1 INTRODUCTION

It is well-known that massive quiescent galaxies are more predominant in the centres of galaxy clusters relative to the general fields in the present day. This trend is often characterized by colours (de Vaucouleurs [1961](#); Visvanathan & Sandage [1977](#); Butcher & Oemler [1984](#); Bower, Lucey & Ellis [1992](#); Bower, Kodama & Terlevich

[1998](#); Terlevich, Caldwell & Bower [2001](#); Tanaka et al. [2005](#); Kodama et al. [2007](#); Bamford et al. [2009](#); Mei et al. [2009](#); Peng et al. [2010](#); Muzzin et al. [2012](#); Wetzel, Tinker & Conroy [2012](#); Darvish et al. [2016](#)) and morphological types (Dressler [1980](#); Dressler et al. [1997](#); Couch et al. [1998](#); Goto et al. [2003](#); Kauffmann et al. [2004](#); van der Wel [2008](#); Cappellari et al. [2011](#); Houghton et al. [2013](#); Fogarty et al. [2014](#); Brough et al. [2017](#); Lopes, Ribeiro & Rembold [2017](#)). Over 10 billion years ago, the most massive structures in the Universe – galaxy protoclusters – played a prominent role in the star formation and mass assembly of massive galaxies

⋆ E-mail: rhythm.shimakawa@nao.ac.jp

(Chiang et al. 2017). Massive protoclusters[1] (van Albada 1961; Peebles 1970; Sunyaev & Zeldovich 1972) at redshift $z \sim 2$–3 are ideal test-beds to probe this rapid transition, and thus develop our understanding of which physical phenomena have driven such early and/or fast growth in centres of distant galaxy clusters (Steidel et al. 2005; Doherty et al. 2010; Tanaka et al. 2010; Gobat et al. 2011; Hatch et al. 2011; Tanaka et al. 2013; Koyama et al. 2013b; Kubo et al. 2013; Alexander et al. 2016; Kubo et al. 2017; Shimakawa et al. 2018).

The rapid change of star formation rate (SFR) density in the centres of clusters seems to follow $(1 + z)^{6 \sim 8}$ from $z \sim 2$ to now (Kodama & Bower 2001; Clements et al. 2014; Smail et al. 2014; Shimakawa et al. 2014; Kato et al. 2016). Such a drastic variation is not only due to the increase in the number of quenched galaxies in clusters at lower redshifts (Blanton & Moustakas 2009; Muzzin et al. 2012; Wetzel et al. 2012; van der Burg et al. 2013; Darvish et al. 2016; Paulino-Afonso et al. 2018) but also due to very active star formation in high-z protoclusters (Dannerbauer et al. 2014; Tadaki et al. 2015; Umehata et al. 2015; Wang et al. 2016; Oteo et al. 2018). These populations are complicated to reproduce with the classical semi-analytic models (Romeo et al. 2015). Moreover, past studies have reported protoclusters which host large numbers of active galactic nuclei (AGNs) (e.g. Lehmer et al. 2009, 2013; Hennawi et al. 2015; Cai et al. 2017; Krishnan et al. 2017, but see Macuga et al. 2018) including radio-loud sources (Pentericci et al. 2002; Röttgering et al. 2003; Venemans et al. 2007; Hatch et al. 2014). A few studies have investigated the energy injection from central AGNs into the ambient gas surrounding high-z (proto-) clusters (Nesvadba et al. 2006; Valentino et al. 2016). There is no good understanding of how large an impact AGNs have on the proto-intercluster medium of protocluster members. This uncertainty makes it even more difficult to understand the mechanism behind the difference in star formation histories in and outside cluster centres.

It is, therefore, important to characterize massive galaxies in protoclusters. Our MAHALO-Subaru (Mapping H-Alpha and Lines of Oxygen with Subaru; Kodama et al. 2013) surveys have extensively studied star formation in high-z clusters and protoclusters. High-density sampling of line emitters at limited redshift ranges ($\pm 2000 \, \mathrm{km \, s^{-1}}$) with narrow-band filters have found the inside-out propagation of star formation and mapped bottom-up structure growth based on the spatial distributions of emission line galaxies and their physical properties. We have identified that the regions dominated by bright line emitters are shifted from the densest cluster cores to lower density outskirts and filamentary outer structures, on time-scales from $z \sim 3$ to present (e.g. Hayashi et al. 2010; Koyama et al. 2010, 2011; Hayashi et al. 2012; Tadaki et al. 2012; Koyama et al. 2013a).

Recent deep follow-up Hα imaging towards a young protocluster, USS 1558 − 003 at $z = 2.53$, finds enhanced star formation and concentration of massive Hα emitters (HAEs) in fragmented group cores (Shimakawa et al. 2018). Furthermore, a follow-up sub-mm/radio campaign with ALMA has shown gas-depleted massive galaxies in the very centre of an X-ray cluster, XMMXCS J2215.9 − 1738 at $z = 1.46$ (Hayashi et al. 2017). Their typical gas fraction is

no more than 10 per cent as opposed to gas-rich sources in the outer regions with gas fractions of $\gtrsim 50$ per cent (Hayashi et al. 2018b, see also Noble et al. 2017). Such a sharp contrast in time and radial distribution would require, e.g. a strong quenching mechanism like AGN feedback (Springel, Di Matteo & Hernquist 2005a; Sijacki et al. 2007; Fabjan et al. 2010; McCarthy et al. 2010; Barnes et al. 2017), and/or rapid gas consumption via starbursts (Hopkins et al. 2009; Hayward et al. 2011; Hopkins et al. 2013; Narayanan et al. 2015).

Here, in the second part of our MAHALO-Deep cluster survey (MDCS), we investigate the properties of massive galaxies in a protocluster associated with a radio galaxy, PKS 1138 − 262 at $z = 2.16$. This protocluster is known to have an apparent red sequence (Kurk et al. 2004a; Kodama et al. 2007; Tanaka et al. 2013); at the same time, there is a strong excess of red Hα-emitting galaxies (Koyama et al. 2013a). Koyama et al. (2013a) also found higher fractions of redder and more massive HAEs in higher-density regions than in under dense regions in the protocluster, implying that the build-up of stellar mass has mostly completed for massive galaxies in the densest parts of the protocluster at this time (see also Doherty et al. 2010; Hatch et al. 2011; Tanaka et al. 2013). These unique trends suggest that the protocluster is in a critical transition phase from young, fragmented, protoclusters, to the classical X-ray clusters at $z \lesssim 2$. The primary goal of this paper is to determine the stellar mass function of protocluster members and then quantify passive fraction and AGN fraction as a function of stellar mass. Also, based on multi-wavelength data sets from literature, we investigate local number densities, rest-frame colours, and SFRs for individual HAEs and check if properties of HAEs are different from the field. These will enable us to investigate how galaxies in the protocluster stop forming stars.

We assume the cosmological parameters of $\Omega_M = 0.3$, $\Omega_\Lambda = 0.7$, and $h = 0.7$ and adopt a Chabrier (2003) stellar initial mass function. The AB magnitude system (Oke & Gunn 1983) is employed throughout the paper.

2 TARGET AND DATA SET

2.1 PKS 1138 − 262

This paper focuses on a dense protocluster associated with a radio galaxy, PKS 1138 − 262 (or MRC 1138 − 262, $\alpha_{J2000} = 11^h 40^m 48^s$, $\delta_{J2000} = -26^d 29^m 09^s$, Bolton, Savage & Wright 1979; Roettgering et al. 1994, 1997; Carilli et al. 1997) at $z = 2.156$ known as the Spiderweb galaxy (Pentericci et al. 1998; Miley et al. 2006). The PKS 1138 protocluster (hereafter PKS 1138) was first explored by Pentericci et al. (1997), Kurk et al. (2000), and Pentericci et al. (2000). PKS 1138, together with the SSA22 protocluster at $z = 3.09$ (Steidel et al. 1998, 2000), has been extensively studied over a long period. The following is a short summary of previous findings on PKS 1138 over the past two decades.

Since the X-ray gas density of nearby galaxy clusters is correlated with the large rotation measures (Taylor, Barton & Ge 1994), Carilli et al. (1997) and Pentericci et al. (1997) have suggested that the Spiderweb galaxy resides in a dense cluster environment given its observed very high rotation measure of the polarized radio emission (6200 rad m^{-2}; see also Athreya et al. 1998).

Kurk et al. (2000) and their series of papers (Pentericci et al. 2000; Kurk et al. 2003, 2004a,b; Croft et al. 2005) identified a significant overdensity in this field based on imaging and follow-up spectroscopic searches towards Lyα and Hα emitters (LAEs and HAEs, respectively) and distant red galaxies (DRGs). Their

---

[1] Various survey bias and restrictions result in vague and inconsistent definitions of the *protocluster* in any work. This series of papers refers to overdense fields on the scale of $\gtrsim 10$, ~ 1–10, and $\lesssim 1$ comoving Mpc as large-scale structures, protoclusters, and dense cores (groups) for the target, respectively.

Table 1. Data summary. The first to fourth columns indicate filter name, instrument/telescope, seeing FWHM, 3σ limiting magnitude in 1.4 arcsec diameter aperture including galactic extinction correction, respectively. The fifth column shows the galactic extinction based on the NASA Extragalactic Database extinction law calculator (Schlegel, Finkbeiner & Davis 1998; Fitzpatrick 1999)[a]. We employ recalibrated estimates from Schlafly & Finkbeiner (2011).

Filter	Instrument /Telescope	FWHM (arcsec)	3σ (AB)	A_λ (mag)
NB_{2071}	MOIRCS/Subaru	0.63	23.95	0.01
K_s	MOIRCS/Subaru	0.63	23.99	0.01
B	S-Cam/Subaru	1.15	26.56[c]	0.14
$F814W$	ACS/*HST*	0.11	26.33[b]	0.06
$F475W$	ACS/*HST*	0.11	27.02[b]	0.13
z'	S-Cam/Subaru	0.70	26.35	0.05
Y	HAWK-I/VLT	0.37	26.08[b]	0.04
J	MOIRCS/Subaru	0.69	24.33	0.03
H	HAWK-I/VLT	0.49	25.11[b]	0.02
K_s	HAWK-I/VLT	0.38	24.75[b]	0.01
3.6 μm	IRAC/Spitzer	1.8	21.42[d]	0.00
4.5 μm	IRAC/Spitzer	1.8	21.57[d]	0.00

Notes. [a] http://irsa.ipac.caltech.edu/applications/DUST/.
[b] Limiting magnitudes after point-spread-function (PSF) matching with NB_{2071}.
[c] Limiting magnitude in 2.5 arcsec aperture diameter.
[d] Limiting magnitude in 8.0 arcsec aperture diameter.

narrow-band imaging surveys succeeded in selecting 50 LAE and 40 HAE candidates, and then spectroscopically confirmed 14 and 9 objects, respectively. They also found high concentrations of HAEs and DRGs within 0.5 Mpc of the Spiderweb galaxy, which are four to five times greater than those outside the central region. Such massive overdensities have been subsequently confirmed on higher dynamic-scales (Koyama et al. 2013a; Shimakawa et al. 2014) and by comparing with other radio galaxy environments (Venemans et al. 2007; Galametz et al. 2012; Mayo et al. 2012). Spectroscopic observations tentatively suggested that the protocluster centre of PKS 1138 may have halo mass $\sim 10^{14}$ M$_\odot$ and virial radius of 0.5 Mpc (Pentericci et al. 2000; Kuiper et al. 2011; Shimakawa et al. 2014) assuming that the system is collapsed (but see Kuiper et al. 2011). Such a massive overdensity has the potential to grow into a massive, Coma-like, galaxy cluster by the present-day (Chiang, Overzier & Gebhardt 2013; Lovell, Thomas & Wilkins 2018).

2.2 Data

We employ the multi broad-band and narrow-band data set from MDCS and the literature. The data consist of B, $F475W$, $F814W$, z', Y, J, H, $K_{s, \mathrm{MOIRCS}}$ (hereafter K_s), $K_{s, \mathrm{HAWKI}}$, and NB_{2071}. Table 1 summarizes the seeing FWHM and limiting magnitudes for these images. The z', J, K_s, and NB_{2071} images are based on the past MAHALO-Subaru campaign (S10B-028I, Kodama et al.; Koyama et al. 2013a) and MDCS (S15A-047, Kodama et al.). The reduced B-band image is provided by Koyama et al. (in preparation), and was recently obtained with Suprime-Cam on the Subaru Telescope between May and June 2017. The narrow-band filter, NB_{2071} has a central wavelength of 2.071 μm with the full width at half-maximum (FWHM) of 270 Å, which covers the H α-redshift 2.15 $\pm$ 0.02 (Fig. 1).

In addition, we use the reduced *Hubble Space Telescope* (*HST*) ACS/WFC data ($F475W$, $F814W$), obtained from the Hubble Legacy Archive (HLA), and reduced near-infrared (NIR) images
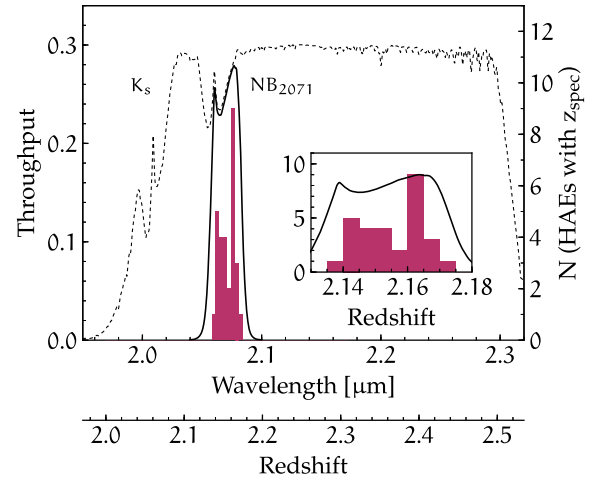
Figure 1. System throughputs of NB_{2071} and K_s filters with MOIRCS, represented by the black solid and dotted lines, respectively. The red histogram shows spec-z distribution of 29 HAEs, 23 of which have been confirmed by Shimakawa et al. (2014); spectroscopic redshifts for the remainder are taken from the literature (Pentericci et al. 2002; Kurk et al. 2004b; Croft et al. 2005; Doherty et al. 2010; Tanaka et al. 2013). One should note that a strong dip at $z \sim 2.16$ is caused by the strong OH lines at $\lambda = 2.0729$ μm preventing us from spectroscopically identifying the H α line of HAEs at this redshift (Shimakawa et al. 2014).

(Y, H, $K_{s, \mathrm{HAWKI}}$) taken with HAWK-I on Very Large Telescope (VLT). These original data have been reported in detail by Miley et al. (2006) and Dannerbauer et al. (2017), respectively. Moreover, this work employs 3.6 and 4.5 μm IRAC bands (Seymour et al. 2007). We use the Post-BCD (PBCD) products from the Spitzer data archive library. Each IRAC band covers 89 per cent of the entire narrow-band emitters. The IRAC images are shallow (21.4–21.6 in 3σ limiting magnitude), and we confirmed that has a negligible effect on the measurement of physical properties with the SED fitting (Section 2.4.1). However, we solely use the photometry in these bands to impose restrictions on the rest-frame NIR spectra of the targeting HAEs at $z = 2.2$; this is crucial when constraining the rest-frame J band magnitudes (Section 3.2).

We also introduce here NB_{2071} data, taken as part of the MDCS with the Multi-Object Infrared Camera and Spectrograph (MOIRCS; Ichikawa et al. 2006; Suzuki et al. 2008) on the Subaru Telescope (the same instrument that was used in the past MAHALO-Subaru survey; Koyama et al. 2013a). The observations were executed between April 30 and May 6, 2015, under photometric conditions with seeing FWHM ~0.6 arcsec. The integration time is 125 min which was split into 180 s individual exposures. After combining with the existing NB_{2071} data (186 min integration), we reconstructed all the data using the reduction pipeline MCSRED[2] (Tanaka et al. 2011), which is written as IRAF[3] scripts (Tody 1993). As described in Shimakawa et al. (2018), we executed flat-fielding, masking objects from the combined data in the first run (thus the whole reduction process was conducted twice to remake secure object masks), sky subtraction (by median sky and then the polynomially fitted plane for residual sky subtraction), distortion correction, cross-matching, and image mosaicing with this pipeline. The reconstructed NB_{2071} image reaches 23.95 mag in 3σ limit-

[2] http://www.naoj.org/staff/ichi/MCSRED/mcsred.html
[3] http://iraf.noao.edu

ing magnitude using a 1.4 arcsec diameter aperture, and its seeing FWHM is 0.63 arcsec. The image depth becomes deeper by 0.5 mag than the previous data (Koyama et al. 2013a). The world coordinate system (WCS, Calabretta & Greisen 2002; Greisen & Calabretta 2002) of the narrow-band image is carefully matched by the IRAF scripts (CCMAP and CCSETWCS) to that of the F814W image, based on 67 point sources. F814W has one of the best spatial resolutions amongst our data set. The standard deviation of point source separations between the NB_{2071} and F814 images suggests that the relative WCS uncertainty would be around 0.04 arcsec in the survey area. One should note, however, that the absolute astrometry would have 0.3 arcsec errors in right ascension and declination based on comparison with the Guide Star Catalogue 2 (Lasker et al. 2008).

2.3 Sample selection

2.3.1 Narrow-band selection

We selected the sample of HAEs by the combined technique of narrow-band selection (Bunker et al. 1995) and $Bz'K_s$ colour selection (Daddi et al. 2004). The former selection is defined by the following criteria:

$$K_s - NB > -2.5 \log(1 - \Sigma\delta 10^{-0.4(ZP-NB)}) + \zeta, \qquad (1)$$

$$K_s - NB > 0.253, \qquad (2)$$

where Σ is the confidence level (in sigma) of the colour-excess and δ is defined by the combined 1σ background noise at NB ($\equiv NB_{2071}$) and K_s bands, ($\delta = \sqrt{\sigma_{NB}(S)^2 + \sigma_{Ks}(S)^2}$, where S is the photometric aperture area), ZP is the zero-point magnitude of the NB_{2071} image, ζ is a correction factor of the colour term. We use $\zeta = -0.04$ which corresponds to the median value of the colour terms in the entire HAEs (Appendix A). The former equation reflects the narrow-band flux limit ($>3 \times 10^{-17}$ erg s^{-1} cm^{-2}) and the latter colour threshold (equation 2) corresponds to the equivalent width limit of narrow-band flux (EW$_{NB}$ = 30 Å in the rest frame for z = 2.15). The EW$_{NB}$ limit is chosen so as not to accidentally pick up contaminant non-emitters (Appendix A).

We note that the measurement of background noise ($\sigma(S)$) in this work and recent other narrow-band studies (e.g. Hayashi et al. 2010; Matthee et al. 2017; Hayashi et al. 2018a) is different from the original calculation by Bunker et al. (1995). Bunker et al. (1995) define the noise by $\sigma(S) = \sqrt{\pi r^2}\sigma_0^2$, where r is an aperture radius and σ_0 is 1σ background noise in pixel. This definition assumes that photometric error is proportional to the aperture radius, however, the real science images have pixel-to-pixel correlations (see e.g. Skelton et al. 2014), which lead to underestimated background noise especially in the larger aperture area. We indeed obtained the power law functions $N = 1.412$ and 1.345 (N is defined by $\sigma(S) \propto r^N$) at NB_{2071} and K_s images based on randomly positioned empty apertures with different radii across the image. This work thus employs the fixed background noise at each band ($NB_{2071, 1\sigma} = 25.14$ mag and $K_{s, 1\sigma} = 25.18$ mag), derived by placing random empty apertures with the same diameter (1.4 arcsec) in the selection process. We here ignore the local sky variance that is estimated to be ≤ 0.1 mag across each image.

We performed source detection in the reduced narrow-band image, using SExtractor (ver. 2.19.5, Bertin & Arnouts 1996). We set detection parameters of DETECT_MINAREA= 9, DETECT_THRESH = 1.2, ANALYSIS_THRESH =1.2, and DEBLEN_MINCONT = 1 × 10^{-4}. K_s-band photometry was conducted by the double-image mode of
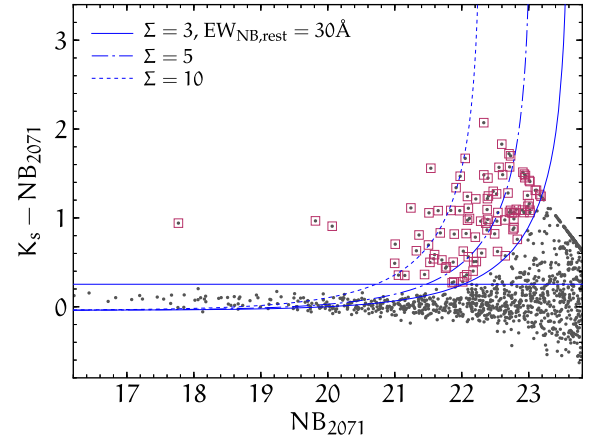
Figure 2. Colour–magnitude diagram, NB_{2071} versus $K_s - NB_{2071}$. The black dots are all NB-detected sources. The red squares indicate narrow-band emitters showing their narrow-band flux excesses greater than three-sigma levels and EW$_{NB}$ higher than 94.5 Å (30 Å in the rest frame at z = 2.15). Blue solid, dash-dotted, and dotted lines are 3, 5, and 10 Σ excess, respectively. The blue horizontal line shows the EW limit.

the SExtractor with the NB_{2071} image for the source detection. Input parameters for source photometry are set with BACK_SIZE= 64, BACK_FILTERSIZE= 5, BACKPHOTO_TYPE = LOCAL, and BACK-PHOTO_THICK = 32 (the same applies all source photometric processes hereafter). According to the Monte Carlo simulation with randomly positioned PSF models embedded in the narrow-band image (see Appendix B for details), the magnitude limit of 95 per cent completeness in the source detection is ~22.8 mag.

Fig. 2 shows the colour–magnitude diagram (NB_{2071} versus $K_s - NB_{2071}$) for NB_{2071}-detected sources in the PKS 1138 region. One should note here that their NB_{2071} magnitudes and colours are based on the fixed aperture photometry of 1.4 arcsec diameter. We assume two-sigma limiting magnitude for non-detections at K_s band. We then select the objects with $\Sigma > 3$ colour-excesses as our narrow-band emitter (NBE) sample. The $\Sigma = 3$ limit in this work is more conservative when compared to $\Sigma = 2$ in Kurk et al. (2004a) and $\Sigma = 2.5$ in Koyama et al. (2013a) for the same field. Nevertheless, thanks to the deeper observing depth than the previous work, $\gtrsim$ 1.5 times more emitters (97 samples) meet our colour criteria in the same area. Our Monte Carlo simulation claims that this narrow-band selection has 68 and 95 per cent completeness at NB_{2071} = 22.80 and 22.45 mag, respectively (Appendix B).

2.3.2 Colour selection

Combined with the past spectroscopic observations (Pentericci et al. 2002; Kurk et al. 2004b; Croft et al. 2005; Doherty et al. 2010; Tanaka et al. 2013; Shimakawa et al. 2014) and narrow-band Ly α imaging (Kurk et al. 2000), we already have 36 secure HAE sources with spectroscopic confirmation or narrow-band excess in two filters in H α and Ly α lines. For the remaining NBEs, even though the survey field is known to be a massive overdense region, it is important to carry out further selection to select HAEs more likely to be associated with PKS 1138 at $z = 2.2$, and exclude other line contaminants. e.g. background [O III], H β line emitters at $z > 3$ and foreground Paα emitter at $z = 0.1$.

Colour–colour selection has been widely used for further selection to remove other line contaminants (Koyama et al. 2013a; Tadaki
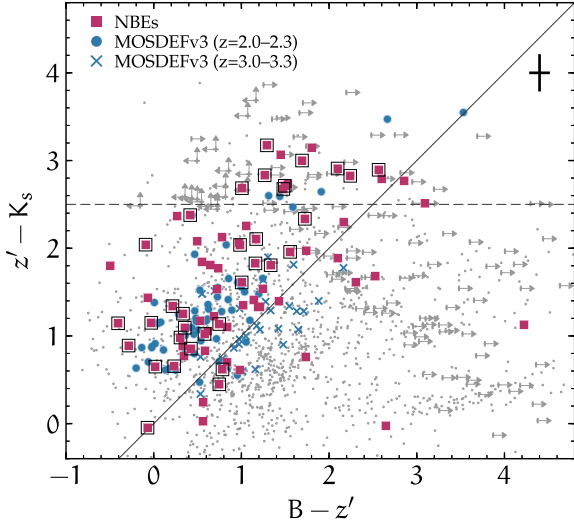
Figure 3. $Bz'K_s$ colour–colour diagram for the PKS 1138 region. Red squares and blue symbols indicate the narrow-band emitters and the spec-z samples at $z = 2.0$–2.3 (circles) and 3.0–3.3 (crosses) from the MOSDEF survey (Kriek et al. 2015), respectively. Spectroscopically confirmed HAEs are highlighted by open black squares. Grey dots are NB-detected sources. The figure only shows objects with $>2\sigma$ detection at K_s-band. Two-sigma-limiting magnitudes replace band photometry for faint sources at B or z'-band. The black solid line is our colour threshold defined to remove those foreground or background contaminants. The horizontal dashed line is the colour criterion of DRG. The black cross on the upper right shows the typical 1σ photometric error of the narrow-band emitters.

et al. 2013). Although it would be better to also integrate with photometric redshifts as demonstrated by the High-redshift(Z) Emission Line Survey (HiZELS; Geach et al. 2008; Sobral et al. 2013), this work does not employ photometric redshifts since available photometric bands are not many as used in such large panoramic surveys. For $z \sim 2.2$ sources, we employ the well known $BzK (\equiv (z - K_s) - (B - z))$ selection (Daddi et al. 2004, 2005) which is accessible given our imaging data set ($Bz'K_s$) as employed in the previous work (Koyama et al. 2013a). The BzK colour criteria enable culling of star-forming and passive galaxies at $z \sim 1.4$–2.5 without extinction correction. We plot NB detections with $>2\sigma$ detection at K_s band on the $Bz'K_s$ colour–colour diagram (Fig. 3). In addition, we also show spec-z sources in the COSMOS–CANDELS field (Capak et al. 2007; Scoville et al. 2007; Grogin et al. 2011; Koekemoer et al. 2011) from the MOSFIRE Deep Evolution Field survey (MOSDEF; Kriek et al. 2015) as a reference sample. $Bz'K_s$ colours of these spec-z sources are derived from the 3D-*HST* database (Brammer et al. 2012; Skelton et al. 2014), which were originally taken by the large legacy surveys with the Subaru Telescope and Vista (Taniguchi et al. 2007; McCracken et al. 2012).

We derive $Bz'K_s$ colours of NB-detections based on the output from the SExtractor (MAG_AUTO) with double-image mode. All images were tailored to the size of the narrow-band image with a scale of 0.117 arcsec per pixel. We employ the outputs of MAG_AUTO in each band and we set KRON_FACT =2.5. One should note that source photometry for the B-band image with a much larger seeing FWHM (Table 1) was also executed independently and then we chose brighter B-band flux densities from single- or double-image mode for individual sources. Based on colours of confirmed members and spec-z sources, we set the colour thresholds of $Bz'K_s > 0$

Table 2. Classification of NBEs and DRG$_{nIR}$ samples in the PKS 1138 region. This work employs confirmed and colour-selected emitters as the HAE sample. We also use HAE candidates when we derive distribution functions (Section 3.4). See Section 2.3 for details.

Class	N	Description
NBEs	97	Narrow-band emitters ($\Sigma > 3$)
HAEs (confirmed)	36	Confirmed by spec-z or Lyα line
HAEs (by colours)	32	Selected by $Bz'K_s$ colour
other line emitters	16	Rejected by $Bz'K_s$ colour
HAEs	68	Confirmed + colour-selected HAEs
HAE candidates	13	Cannot be rejected by colours
DRG$_{nIR}$	34	$z' - K_s > 2.5$ w/o 24 µm detection

or ($z' - K_s$) >2.5, and then select an additional 32 HAE members as well as remove 16 narrow-band emitters as other line emitters (Table 2). Here, we adopt a $Bz'K_s$ colour criterion that is different from the Daddi et al. (2004) prescription ($BzK \geq -0.2$). We assume two-sigma-limiting magnitudes for non-detections, and then evaluate them if those upper limits or lower limits can meet our selection criteria. The $Bz'K_s$ selection cannot perfectly guarantee that the selected NBEs are our targeting HAEs at $z = 2.15 \pm 0.02$ though (Fig. 3). We indeed find that two confirmed protocluster members drop below our selection limit. On the other hand, some reference spec-z sources at $z = 3.0$–3.3 break into the realm of $Bz'K_s$-selected galaxies. Also, colour-selected HAEs and rejected line emitters near boundaries of the colour criteria cannot be securely classified once we take account of those photometric errors. While we count these colour-selected emitters as HAEs throughout this paper at this time, we definitely require follow-up spectroscopy for the robust identification of these sources in the future. The on-line catalogue (Appendix C) summarizes the identification status for individual HAE samples in detail.

When taken together, a total number of 68 HAEs have been selected as the protocluster members in this work. Out of these, 51 were already discovered by our previous survey (Koyama et al. 2013a), meaning that our deeper data increase the number of the HAE sample by 33 per cent. Besides these, we have 13 NBEs which cannot be removed by the $Bz'K_s$ colour due to insufficient photometric data. These unknown emitter samples are defined as HAE candidates. Given the ten times higher density in the protocluster region (Section 3.4), most of these faint emitters should be HAEs. The contamination rate in the HAE candidates may be around $\sim$20 per cent considering 16 colour-rejected NBEs amongst the 84 (36 + 32 + 16) emitters (Table 2).

2.3.3 Distant red galaxies (DRGs)

We also establish a reference sample of distant red galaxies (DRGs) that do not show signs of active star formation. These objects allow us to infer the selection bias of our narrow-band technique at the massive end, and also provide the upper limit to the quiescent population in the derivation of the stellar mass function (Section 3.1). We first choose objects with significant K_s-band detection, $K_s < 23.4$ (5σ limit mag), corresponding to the 95 per cent completeness limit for massive galaxies ($M_\star > 10^{10.5}$ M$_\odot$) according to the photo-z source catalogue in the COSMOS field (Laigle et al. 2016). We then select passive BzK (pBzK) galaxies that satisfy ($z' - K_s$) >2.5 (Fig. 3) and do not overlap with NBEs nor MIPS/Spitzer 24

μm sources reported by Koyama et al. (2013a). One should note that this colour threshold is different from the classic definition of DRGs ($J − K_s > 2.3$ in vega) by van Dokkum et al. (2004) and Franx et al. (2003). The cross-checking with MIPS 24 μm sources allows us to remove significant dusty starburst populations. The detection limit at the MIPS 24 μm image roughly corresponds to the infrared luminosity of $L_{IR} \sim 10^{12}\, L_\odot$ and SFR $\sim 100\, M_\odot\, yr^{-1}$ at $z = 2.15$.

This selection results in 34 DRG$_{nIR}$ candidates without bright-IR emission ($L_{IR} \gtrsim 10^{12}\, L_\odot$), which are described as DRG$_{nIR}$ hereafter. Three of these are known to be protocluster members confirmed with spectrophotometric analysis (Tanaka et al. 2013). According to a photometric redshift code, EAZY (Brammer, van Dokkum & Coppi 2008; Brammer et al. 2011), measured photometric redshifts fall within $z = 2.1 \pm 0.2$ in 17 sources.

2.3.4 X-ray sources

We checked the presence of X-ray emission from our HAE samples using an image from the Chandra X-ray Observatory. Our survey field is covered by the S3 chip with the ACIS-S detector. The data quality and source catalogue were published in Carilli et al. (2002) and Pentericci et al. (2002). However, we double-checked the data independently based on the Chandra Source Catalogue (CSC v1.1, Evans et al. 2010) and also by analysing the original data with the Chandra Interactive Analysis of Observations (CIAO v4.7.6) to obtain more detailed coordinates.

Based on X-ray detections selected by the CIAO code WAVDE-TECT for an exposure-weighted reduced image with MKEXPMAP, we found that six HAEs (#40,46,58,68,73,95) have X-ray detections within 0.4 arcsec separation angle at higher than four-sigma levels. The faintest X-ray source has 4×10^{-15} erg s^{-1} cm^{-2} and 1.4×10^{44} erg s^{-1} in unabsorbed flux and luminosity (assuming the redshift of $z = 2.15$) at the broad-band (0.5–7.0 keV) according to the CSC, respectively. Given such a shallow detection limit, these X-ray sources are expected to originate from active galactic nuclei. All of these X-ray sources have been identified as #3,5,6,7,16 in Pentericci et al. (2002), whereas #7 contains two HAE sources defined in this work: one is the Spiderweb radio galaxy (#73 in this work), and the other is HAE-058. Corresponding identification numbers to each HAE are fully described in our catalogue (Appendix C).

2.3.5 Other resources

The Spiderweb protocluster is a well-surveyed region, with numerous studies in addition to those already mentioned, e.g. MIPS 24 μm imaging with the Spitzer Space Telescope (Mayo et al. 2012; Koyama et al. 2013a,b), LABOCA 870 μm imaging with the APEX telescope (Dannerbauer et al. 2014), CO(1 − 0) observation with ATCA (Emonts et al. 2016; Dannerbauer et al. 2017; Emonts et al. 2018), and CO(3 − 2) observation with ALMA (Tadaki et al., in preparation).

Because of the restricted field coverage relative to our survey area, or serious blending issue due to poor spatial resolutions, we do not use these other resources, mostly in the mid-IR to radio regime, unless otherwise mentioned. On the other hand, these past studies are useful to characterize some specific HAEs, and thus, such information is referenced where appropriate throughout the paper.

2.4 Derivation of physical properties

This section explains how we derive line flux, stellar mass, and amount of dust reddening. The measuring methods are similar to those in the first paper of the MDCS series (Shimakawa et al. 2018).

2.4.1 SED fitting

We use SED-fitting to derive stellar masses and dust extinctions of our samples based on the SED-fitting code (FAST) distributed by Kriek et al. (2009). We use the Bruzual & Charlot (2003) stellar population model, the Calzetti et al. (2000) extinction law, and the Chabrier (2003) IMF. We then run the code with a fixed redshift of $z = 2.15$ independently of spectroscopic confirmation and low metal abundance of $Z = 0.004$ ($0.2\, Z_\odot$), and assume delayed exponentially declining star formation history (SFR $\propto t \cdot exp(− t/\tau)$). τ value and age are allowed to be $10^9–10^{11}$ yr and $10^{7.6}–10^{9.4}$ yr, respectively. We allow the amount of stellar extinction (A_V) to be between 0 and 3 mag. The outcome of the choice of these parameter sets does not significantly affect the stellar mass estimations. However, the obtained dust extinction systematically depends on input parameters. If we employ solar metal abundance instead of $Z = 0.2\, Z_\odot$, for instance, derived A_V values become systematically lower by 0.2–0.3 mag than those with $Z = 0.004$. Indeed, dust correction is the major issue for narrow-band studies due to the lack of H β line information. Considering this model dependency, we pay special attention to physical properties requiring dust correction, such as SFR, throughout the paper.

We then carried out the SED fitting based on multi-band photometry derived in the same way as for the $Bz'K_s$ colour estimation in the previous subsection. First, we performed PSF-matching for the $F475W$, $F814W$, Y, H, $K_{s, HAWKI}$ images to the seeing size of NB_{2071}. Source photometry at IRAC 3.6 and 4.5 μm bands were conducted independently, and we cross-matched those to NBEs within 1 arcsec distance. Whilst we executed the SED-fitting with IRAC photometry if available, we confirm that IRAC data have negligible effects on stellar mass and A_v estimation in our samples. This lack of systematic discrepancy regardless of the availability of IRAC photometry is consistent with past work (Elsner, Feulner & Hopp 2008; Muzzin et al. 2009). Derived stellar masses and dust reddening are summarized in Appendix C. We employ 1σ errors of obtained parameters from 100 Monte Carlo simulations carried out with the FAST code.

Typical fitted SED spectra of massive HAEs ($M_\star > 10^{10.5}\, M_\odot$) are presented in Fig. 4, which are divided into the spectra of HAEs with or without X-ray counterparts. We should note that, in spite of the importance of the SED decomposition into the stellar light and the nuclear component (Merloni et al. 2010; Santini et al. 2012), this work ignores this procedure due to the lack of photometric bands at rest-frame IR bands. Although we have Spitzer/MIPS 24 μm data, the serious blending issue does not provide us with reliable mid-IR photometry. At the least, the stellar mass measurement of the Spiderweb radio galaxy, the most luminous X-ray source in our sample, is highly uncertain. Also, we see a clear excess at IRAC bands from the extrapolation of model-inferred SED in one of X-ray HAEs (#58) and whose derived stellar mass should be overestimated as well. For other AGN host HAEs, since their photometry can be fitted only by stellar components, it remains unclear how reliable our stellar mass estimates are. High-resolution deep mid-IR data, by, e.g. JWST/MIRI (Rieke et al. 2015), are needed to decompose those SEDs and obtain pure stellar components.
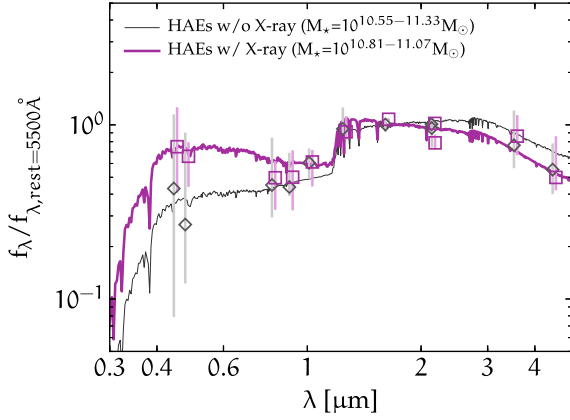
Figure 4. Median stellar spectra of massive ($M_\star > 10^{10.5}$ $M_\odot$) HAEs with and without X-ray emission, which are represented by purple thick and black thin lines, respectively. These are derived from the median values of fitted SED spectra normalized at $\lambda_{\rm rest} = 5500$ Å for individuals. Their median values and 1σ scatters of observed flux densities at 11 photometric bands are shown by purple squares and black diamonds, respectively (the data points are slightly shifted in a transverse direction for better visibility). Minimum–median–maximum values of derived log stellar mass in each group are 10.81–11.01–11.07 in the HAEs with X-ray sources and 10.55–10.77–11.33 in the HAEs without X-ray counterparts.

2.4.2 Narrow-band flux

We obtained narrow-band line flux ($F_{\rm NB}$), emission subtracted flux density at K_s-band (f_c), and rest-frame equivalent width of narrow-band flux ($EW_{\rm NB}$) by the following formula,

$$F_{\rm NB} = \Delta_{\rm NB} \frac{f_{\rm NB} - f_{\rm Ks'}}{1 - \Delta_{\rm NB}/\Delta_{\rm Ks}}, \tag{3}$$

$$f_c = \frac{f_{\rm Ks'} - f_{\rm NB} \cdot \Delta_{\rm NB}/\Delta_{\rm Ks}}{1 - \Delta_{\rm NB}/\Delta_{\rm Ks}}, \tag{4}$$

$$EW_{\rm NB} = \frac{F_{\rm NB}}{f_c \cdot (1 - z)}, \tag{5}$$

where $\Delta_{\rm NB}$ and $\Delta_{\rm Ks}$ are full-width-half-maximum (FWHM) of NB_{2071} (270 Å) and K_s band (3100 Å) filters, respectively. $f_{\rm Ks'}$ is K_s-band flux density including the colour term correction (Section 2.3.1). We employed -0.04 mag for the colour term correction based on the median value of model-inferred SED spectra of the entire HAEs (Fig. A1). Given the similar centre wavelength between the two filters, uncertainty from the colour correction is negligibly small relative to the total flux errors.

On the other hand, the shape of the filter throughput including atmospheric transmission on Maunakea (Fig. 1) may cause an additional $\sim$12 per cent error in the flux estimation according to the standard deviation of the response curve at wavelengths within the filter FWHM. We incorporate this error budget into the narrow-band flux errors of HAEs individually. One should note that we likely overestimate this error value given that HAEs tend to gather towards the protocluster system ($z \sim 2.156$) along the line of sight (Shimakawa et al. 2014).

We then obtained observed H α luminosities of HAEs as follows. We assume a fixed redshift of $z = 2.15$ that corresponds to the H α redshift captured by the centre of the NB_{2071} filter. Flux contribution from the [N II] $\lambda\lambda6550$, 6585 doublet is corrected based on their stellar masses derived by the SED fitting (Section 2.4.1). Our past

spectroscopic observation has derived typical [N II] $\lambda6585$/Hα flux ratios (N2; Pettini & Pagel 2004) for HAEs in PKS 1138 at different stellar mass bins (Shimakawa et al. 2015), which can be characterized by the following relation,

$$N2 = -0.71 + 0.33 \times [\log(M_\star/M_\odot) - 10]. \tag{6}$$

This prescription enables relatively self-consistent N2 correction for the narrow-band flux in our sample. We assume [N II] $\lambda6550$: [N II] $\lambda6585 = 1:3$ to remove [N II] $\lambda6550$ flux as well (Osterbrock 1974). In addition, we incorporate the uncertainty of the N2 correction into the derived H α luminosities based on the typical observational scatter $\Delta \log(O/H)_{\rm N2} \sim 0.1$ dex (i.e. $\Delta N2 = 0.18$ dex) of the N2-inferred mass–metallicity relation (Tremonti et al. 2004; Mannucci et al. 2010; Steidel et al. 2014). The calculated H α luminosities and those total error budgets are summarized in the online catalogue (Appendix C).

3 RESULTS

The goal of this paper is to investigate physical properties of massive HAEs in the Spiderweb protocluster (PKS 1138) at $z = 2.2$. Our previous paper (Shimakawa et al. 2018) reported the vigorous formation of more massive galaxies in fragmented dense groups alongside intergroup regions within the USS 1558 protocluster at $z = 2.53$. Compared to USS 1558, PKS 1138 is apparently a more advanced and reddened protocluster system (Kodama et al. 2007). More specifically, Galametz et al. (2012) have reported three times higher number density of old populations selected by IRAC colour in this field compared to the typical radio galaxy environments at high redshifts including USS 1558. Given the fact that massive galaxies in the protocluster are destined to grow into bright red sequence galaxies in the local Universe, identifying these massive HAEs will help us to infer the evolutionary steps cluster galaxies would have experienced in their maturing phases at $z \sim 2$.

3.1 Stellar mass functions

We first derive the stellar mass function of HAEs in PKS 1138 whose stellar masses are individually derived from the SED fitting. Since the mass estimations do not include the SED decomposition to remove AGN contamination, all results obtained in this section must be taken with caution. Analysing the Spiderweb protocluster region especially suffers from this issue due to the number excess of luminous X-ray sources (Pentericci et al. 2002).

We use the same measuring method as in our previous paper (Shimakawa et al. 2018) for HAEs in USS 1558 protocluster region at $z = 2.53$. The most important part of the derivation of the stellar mass function for narrow-band selected emitters is the completeness correction. Following Shimakawa et al. (2018), we evaluate both detection completeness and selection completeness with the Monte Carlo simulation. The detection completeness is defined as the fraction of missing samples in the source detection process, which is highly dependent on the initial parameters of the SExtractor code (Section 2.3.1). The selection completeness is a specific problem of the narrow-band selection, which is first noted by Sobral et al. (2009) and then developed by their following analyses (Sobral et al. 2012, 2013, 2014). The selection completeness indicates the completeness in the process of the narrow-band colour selection (Section 2.3.1). Evaluating the selection completeness is especially crucial since the narrow-band selection is not only based on the depth of the narrow-band image, but is also dependent on the
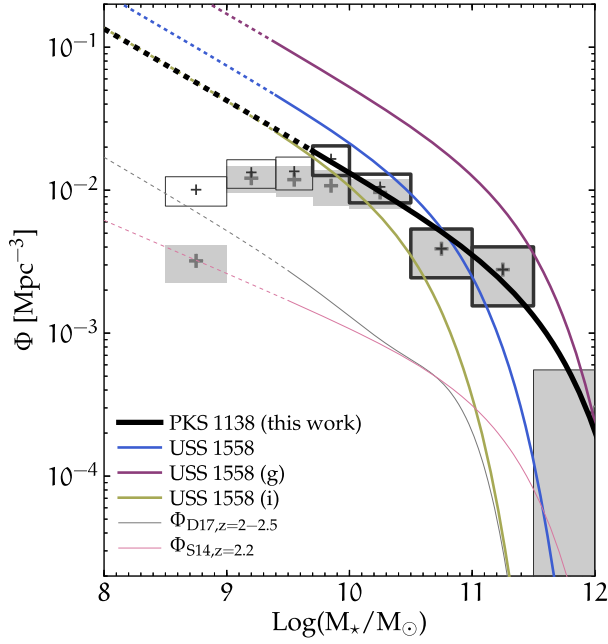
Figure 5. Stellar mass functions in various fields at $z \sim 2$. Open and filled boxes show the number densities with and without completeness correction at each stellar mass bin. The blue curve represents the stellar mass function in the USS 1558 protocluster at $z = 2.5$. Purple and yellow curves are those in the group and intergroup regions therein, respectively. Thin grey and pink lines are the stellar mass function in the general field at $z \sim 2$. The former is based on star-forming galaxies selected from their rest-*UVJ* colours and photo-z (Davidzon et al. 2017). The latter is narrow-band selected HAEs including additional sorting with photo-z and colours (Sobral et al. 2014). Dotted lines indicate the extrapolated lines from the available data range in each function.

colour between narrow-band and broad-band photometry (see Sobral et al. 2009). Indeed, our Monte Carlo analysis indicates that the narrow-band selection requires an additional 20–70 per cent completeness correction at the faint end relative to the completeness correction only for the detection. The detailed procedure of our completeness correction is examined in Appendix B.

Fig. 5 shows the number densities as a function of stellar mass for HAEs in PKS 1138. We evaluate the number densities of HAEs by $\phi(\log L) = \Sigma_i (V_{max} \cdot C(NB) \cdot \Delta(\log L))^{-1}$, where $L = M_\star / M_\odot$ and V_{max} (=3676 co-Mpc^3) is the volume size, respectively. The latter is obtained from the filter FWHM of the narrow-band filter (55 co-Mpc) and the survey area (66 co-Mpc^2). Since the redshift distribution of HAEs is more concentrated around the protocluster centre (Shimakawa et al. 2014), we tend to overestimate the volume size. Open squares in Fig. 5 include the completeness corrections that also incorporate 13 unclassified HAE candidates (Table 2) to compensate loss from the $Bz'K_s$ colour selection. We count these candidates with the additional correction of 20 per cent possible contamination (Section 2.3.2). One should note that while this further correction could affect the resultant fitting parameters, this does not change our conclusion since all HAE candidates are less-massive galaxies at stellar masses lower than $10^{10.5}$ M$_\odot$, most of which are outside of the scope of this work.

We fit the stellar mass distribution using the Schechter function (Schechter 1976), which is given by the following equations,

$$\phi(L)dL = \phi^* \left(\frac{L}{L^*} \right)^\alpha \exp \left(-\frac{L}{L^*} \right) \frac{dL}{L^*}, \, or \quad (7)$$

Table 3. Results of Schechter function fitting for the stellar mass distribution. The third and fourth columns indicate the normalization factors between PKS 1138 and the general fields at the similar redshift range reported by Davidzon et al. (2017) and Sobral et al. (2014) at the stellar mass of $10^{9.7}$ M$_\odot$, respectively.

$\log(M_\star^*/M_\odot)$	$\log(\Phi_{M_\star}^*/Mpc^{-3})$	$\Phi_{9.7}/\Phi_{D17}$	$\Phi_{9.7}/\Phi_{S14}$
11.726 ± 0.756	-3.097 ± 0.432	9.12	13.29

$$\phi(L)dL = \phi^* \left(\frac{L}{L^*} \right)^{\alpha+1} \exp \left(-\frac{L}{L^*} \right) \ln 10 d(\log L), \quad (8)$$

where L^* is the characteristic stellar mass at which the power law slope cuts off. We then fit the stellar mass distribution with the Schechter function based on the MPFIT code (Markwardt 2009).[4] We do not use the stellar mass bins of $10^{8.5-9.7}$ M$_\odot$ in the fitting since we cannot probe typical star-forming galaxies at these bins due to the flux limit (Section 3.3). Also, we remove the radio galaxy ($M_\star = 10^{12.4}$ M$_\odot$). The thick frames in Fig. 5 highlight the sample bins used in the curve fitting.

The derived parameters of the curve fitting are given in Table 3. Due to the small sample size, we fix the powe-law slope to $\alpha = -1.5$, as used in Shimakawa et al. (2018), to minimize the fitting errors. We should note that our restricted sample sizes and large binning sizes would not be sufficient to determine the function parameters and even errors robustly. Indeed, it is known that there are non-negligible variations of derived $M_\star^*$ and Φ_* even if one employs much larger data sets, perhaps due to the cosmic variance and selection effects (Ilbert et al. 2013; Muzzin et al. 2013; Sobral et al. 2014; Davidzon et al. 2017; Hayashi et al. 2018a). Although systematic comparisons are unfair because of such issues, the differences of the number densities between PKS 1138 and the general fields (Sobral et al. 2014; Davidzon et al. 2017) at the stellar mass $\sim 10^{10}$ M$_\odot$ (Fig. 5) suggest that the PKS 1138 protocluster is an approximately ten times higher density region than the general field at a similar redshift.

The figure also shows the stellar mass function of HAEs in the USS 1558 protocluster at $z = 2.53$, and its group regions and intergroup regions (Shimakawa et al. 2018). These functions are derived by the same procedure as this work, which enables a relatively fair comparison between two protoclusters at different redshifts. We find that the cut-off stellar mass of HAEs in PKS 1138 at $z = 2.2$. Whilst the derived cut-off values would be overestimated since we may overestimate stellar masses of AGN host galaxies, this is consistent with that in the fragmented group regions ($M_\star^* \sim 10^{11.5}$ M$_\odot$) in USS 1558 at $z = 2.5$, within the error margins. Both have significantly higher characteristic stellar masses than those in the intergroup regions ($M_\star^* \sim 10^{10.6}$ M$_\odot$) in USS 1558, meaning that PKS 1138 is associated with the larger number of more massive HAEs than lower density regions in USS 1558 at $z = 2.53$. Also, this could suggest that PKS 1138 is at a point where fragmented cores are about to consolidate into a massive cluster with a single core if we assume these two protoclusters are on the similar evolutionary track to massive clusters (Shimakawa et al. 2014). Comparing these two protoclusters in the stellar mass function, the PKS 1138 region has a 1.5 times lower number density of HAEs relative to USS 1558.

We also estimate the fraction of bright X-ray sources among HAEs in each stellar mass bin. Studying AGN activities across

[4]http://purl.com/net/mpfit
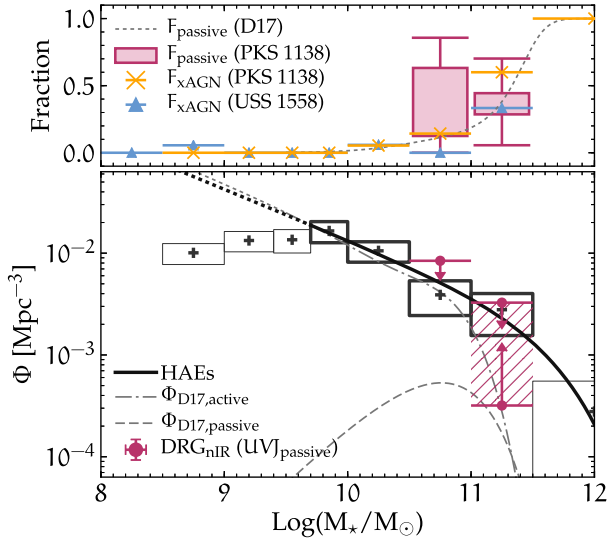
Figure 6. *Lower panel:* Stellar mass function in the PKS 1138 protocluster region (same as in Fig. 5). This figure also plots the 1σ upper limits of the stellar mass function for passive galaxies at $M_\star > 10^{10.5}$ $M_\odot$ based on the DRG$_{nIR}$ samples. We select DRG$_{nIR}$ whose rest-frame *UVJ* colours agree with passive galaxy populations within 1σ errors. The lower limits are constrained by three quiescent objects with spectroscopic (or spectrophotometric) confirmation by Tanaka et al. (2013). Grey dash–dotted and dashed curves are the stellar mass function of star-forming and passive galaxies in the general field at $z = 2$–2.5 (Davidzon et al. 2017). *Upper panel:* Fraction of X-ray selected AGNs among HAEs (orange crosses) and passive galaxies (red hatched region) in PKS 1138 as a function of stellar mass. The latter is calculated based on the 1σ upper and lower limits shown in the lower panel, and error-bars include Poisson noise. Blue triangles indicate the X-ray AGN fraction among HAEs in USS 1558 at $z = 2.53$ (Macuga et al. 2018). The grey dotted line indicates the passive fraction in the general field at $z = 2$–2.5 reported by Davidzon et al. (2017).

different stellar mass ranges is essential since AGNs are thought to have mass dependence and especially play critical roles in massive-end systems (Ferrarese & Merritt 2000; Kauffmann et al. 2003; Di Matteo, Springel & Hernquist 2005). We thus merely check the X-ray AGN fraction in our HAE samples and then find that more than 60 per cent (4/6) of very massive HAEs host AGNs at $M_\star = 10^{11 - 12.5}$ $M_\odot$ (Fig. 6). Such a high AGN fraction may be even more enhanced once we get a better AGN identification tool (see discussion Section 4). The figure also shows AGN fraction in the other protocluster area, USS 1558 at $z = 2.53$ (Macuga et al. 2018). This detection limit of $L_X = 3 \times 10^{43}$ erg s^{-1} is deeper than that in PKS 1138. In USS 1558, despite that, there is no bright X-ray source in a higher density region within the protocluster except the radio galaxy that is the only X-ray source (1/3) in the highest stellar mass bin ($M_\star = 10^{11}$–$10^{11.5}$ $M_\odot$). We summarize the AGN fraction in each stellar mass bin in Table 4.

In addition, we tentatively constrain the quenching fraction in PKS 1138 by combining HAEs with DRG$_{nIR}$ samples (Section 2.3.3). Within the target area, there are 34 DRG$_{nIR}$ sources that do not have flux excesses at narrow-band nor bright dust emission at MIPS/24 μm band, which provide the upper limit of the distribution functions of passive galaxies in PKS 1138. We here employ only DRG$_{nIR}$ that can be classified as passive populations on the rest-frame *UVJ* plane within margins of 1σ errors. Also, three of them are spectroscopically (or spectrophotometrically) identified by Tanaka et al. (2013). They allow us to constrain the lower limit

Table 4. X-ray AGN fractions amongst HAEs in PKS 1138 ($z = 2.15$) and USS 1558 ($z = 2.53$) at different stellar mass bins. One should note that these do not include the HAE candidates and the completeness correction.

$\log(M_\star^*/M_\odot)$	PKS 1138	USS 1558
8.0–8.5	–	0/5 (0%)
8.5–9.0	0/3 (0%)	1/18 (6%)
9.0–9.4	0/14 (0%)	0/21 (0%)
9.4–9.7	0/10 (0%)	0/20 (0%)
9.7–10.0	0/11 (0%)	0/17 (0%)
10.0–10.5	1/17 (6%)	1/18 (6%)
10.5–11.0	1/7 (14%)	0/5 (0%)
11.0–11.5	3/5 (60%)	1*/3 (33%)
11.5–12.5	1*/1 (100%)	–

Note. * Radio galaxies.
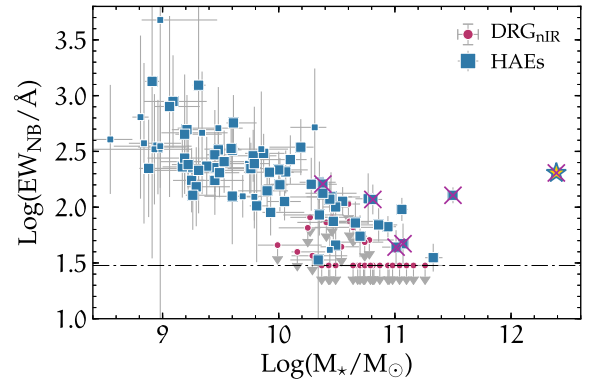
Figure 7. EW of narrow-band flux (EW$_{NB}$) against stellar mass. Blue large and small squares show HAEs and HAE candidates respectively (Table 2). The horizontal dash-dotted line indicates our EW selection limit that corresponds to the rest-frame EW$_{NB}$ = 30 Å at $z = 2.15$. Purple crosses have X-ray counterparts. error-bars show 1σ uncertainties. We also plot upper limits of EW$_{NB}$ for the DRG$_{nIR}$ samples by red circles for a reference.

of number densities of passive objects. We derive their stellar mass from the SED-fitting by assuming the fixed redshift of 2.15 and then employ only the 23 DRG$_{nIR}$ with the stellar mass greater than $10^{10.5}$ $M_\odot$ in this analysis.

Roughly expected number densities of passive galaxies and the passive fraction as a function of the stellar mass can be seen in Fig. 6. The fraction of passive galaxies in PKS 1138 is estimated to be $\sim$36 per cent. One should note that, however, such a constraint becomes almost irrelevant once we include errors. When we compare the number density of our DRG$_{nIR}$ samples at $K_s = 21$–23 mag with that of DRG$_{nIR}$ selected in the same way (§2.3.3) in the COSMOS field (Laigle et al. 2016), the excess factor of DRG$_{nIR}$ in PKS 1138 is estimated to be $\sim$1.7 (which is consistent with the estimation by Kodama et al. 2007). The upper limits of the number densities thus should be overestimated due to the foreground and background contaminants. A future deep NIR survey with instruments such as Keck/MOSFIRE and JWST/NIRSpec is required to obtain the passive fraction more reliably.

Regarding these trends, we caution about a potential issue in our narrow-band selection. Our HAE samples are limited either by the narrow-band flux ($>3 \times 10^{-17}$ erg s^{-1} cm^{-2}) or EW$_{NB}$ (>30 Å in the rest frame) depending on their narrow-band magnitude (Fig. 2). Fig. 7 roughly explains how this selection bias may affect the different stellar mass ranges. Since the narrow-band magnitude correlates with the stellar mass, the flux limit is the primary bias

in the narrow-band selection at the lower stellar mass regime, $\lesssim 10^{10.4}$ M$_\odot$ (i.e. equation 1). On the other hand, towards the massive end (M$_\star \gtrsim 10^{10.4}$ M$_\odot$), the EW$_{NB}$ limit (>30 Å) as defined by equation 2 drives the selection bias. Thus, we should note that our HAE selection is not fully equal to the selection of star-forming populations at the massive end, in the meaning that the selection is restricted by EW$_{NB}$ that roughly corresponds to specific SFR instead of the narrow-band flux (i.e. SFR). Such an additional bias would require special attention when we regard our HAE samples as star-forming galaxies. For example, we may underestimate the number of star-forming galaxies at the massive end. Also, the AGN fraction could be overestimated since EW$_{NB}$ could be enhanced by the flux contribution in both Hα and [N II] lines from AGNs. For reference, Sobral et al. (2016) have found that AGNs contribute ~15 per cent of the total Hα luminosity density at any redshift up to $z = 2.23$. We return to the discussion of the AGN fraction in (Section 4).

Shimakawa et al. (2018) have derived the dust-corrected Hα luminosity function in the USS 1558 field, with tentative extinction correction for individual HAEs. However, we decide not to discuss the Hα luminosity function towards the PKS 1138 region since this protocluster is known to be associated with a large number of dusty starbursts (Stevens et al. 2003; Mayo et al. 2012; Koyama et al. 2013a; Valtchanov et al. 2013; Rigby et al. 2014; Dannerbauer et al. 2014) and it is thus very challenging to properly estimate dust-corrected Hα luminosities for all HAEs on an equitable basis. If we apply dust correction in the same way as for HAEs in the USS 1558 field (Shimakawa et al. 2018), we can derive $\log(L^*_{H\alpha}/\text{erg s}^{-1}) = 43.61 \pm 0.20$ and $\log(\Phi^*_{L_{H\alpha}}/\text{Mpc}^{-3}) = -2.38 \pm 0.18$, respectively.

3.2 Spatial distribution and rest-frame colours

We show the positions of our updated HAE samples over the survey area in Fig. 8. The underlying colour in the figure indicates the excess of the number density ($\log(1 + \delta)$), which is defined by the following equation:

$$\delta = \frac{\Sigma_{5th} - C \cdot \overline{\Sigma}_{5th}}{C \cdot \overline{\Sigma}_{5th}}, \tag{9}$$

where Σ_{Nth} is the surface density in physical (ph-) Mpc^{-2} including N HAEs therein. Here, we adopt $N = 5$. C is the scaling factor which normalizes the mean number density over the entire protocluster field ($\overline{\Sigma}_{5th} = 13.5$ ph-Mpc^{-2}) to the typical density in the general field. We tentatively apply $C = 0.1$ inferred from the 10 times higher number density of the stellar mass function at M$_\star \sim 10^{10}$ M$_\odot$ relative to those in the general fields (Section 3.1).

The PKS 1138 protocluster is associated with a very dense region of HAEs around the Spiderweb galaxy as first reported by Kurk et al. (2004a): it contains more than 100 times as many galaxies as seen in the random field in the local scale (see also Kuiper et al. 2011). We find >10 new Hα detections associated with this massive structure. Also, four out of six HAEs with X-ray detections (Pentericci et al. 2002) are positioned within or close to the central system. PKS 1138 is also known to have filamentary structures on the east side (Croft et al. 2005; Koyama et al. 2013a) which are aligned along the line of sight as well (Shimakawa et al. 2014). The most compact group in this region can be seen at four co-Mpc away eastward from the radio galaxy. This compact group involves four HAEs (#25,26,27,29) within only 60 ph-kpc distance and has a 3.6σ source detection (5.0 $\pm$ 1.4 mJy) at LABOCA 870 μm (#DKB12 in Dannerbauer et al. 2014). The peak density of passive galaxy candidates selected as DRGs is slightly shifted towards the east

direction, though more spectroscopic identifications are needed to confirm this sub-structure.

We then estimate the rest-frame *UVJ* colours, and associated errors, of HAEs using the EAZY code (Brammer et al. 2008, 2011), and then investigate colour dependence on the local scale. The rest *U*, *V*, *J* photometries roughly correspond to *Y*, *H*, and 3.6 μm bands, respectively.

Fig. 9 shows the surface number densities versus the rest-frame $U - V$ colours of HAEs. We explore the colour dependence on local environments with different density measurements, i.e. the surface densities including 5th neighbours, and distance from the radio galaxy (d_{RG}). We find no clear correlation between $U - V$ colours and local densities of HAEs within the protocluster, which is unchanged when we use Σ_{3th} or Σ_{10th} for the density measurement. These results are inconsistent with the concentration of redder HAEs towards the protocluster centre as reported by Koyama et al. (2013a). However, Koyama et al. (2013a) investigated the colour dependence of HAEs in an area twice as large as the survey field of MDCS, and their results are enhanced by the absence of red HAEs in these outer regions. We, therefore, conclude that the inconsistency between this work and Koyama et al. (2013a) is due to the insufficiently large survey area in this work to confirm the finding of Koyama et al. (2013a).

We then characterize HAEs on the rest-frame *UVJ* plane (Fig. 10). The shallow depths of the IRAC bands ($m_{3\sigma} \sim 21.5$ AB), mean that only 32 per cent of the entire HAE sample are detected at IRAC bands at a more than two-sigma confidence level. These IRAC detected HAEs are shown by the filled symbols in Fig. 10. Typical errors are $\Delta(U - V) = 0.31$ dex and $\Delta(V - J) = 0.29$ dex, respectively. The remainders are indicated by open symbols and have rest *J*-band magnitudes estimated from the extrapolated SED spectra. Uncertainties of rest $V - J$ colours in these non-IRAC detections would be ~0.6 dex according to the EAZY code.

As a result, we find that rest-frame *UVJ* colours of HAEs agree with those of the star-forming population (Williams et al. 2009; Moresco et al. 2013; Straatman et al. 2016; Fang et al. 2018) within the margin of error. Despite the significant uncertainties of individual colours, HAEs hosting bright X-ray AGNs tend to have redder rest-frame $U - V$ colours, which agree with the findings by Krishnan et al. (2017). More interestingly, we see that HAEs with X-ray emissions (#40,58,68,73,95) are preferentially located near the edge of the quiescent population. The outlier lying at the bottom on the *UVJ* plane (#46) is known to be an AGN (#6 in Pentericci et al. 2002 and #215 in Kurk et al. 2004b), with very broad Hα line emission identified by near-infrared spectroscopy with VLT/ISAAC (Kurk et al. 2004b). The colour trend suggests that HAEs hosting X-ray AGNs could be in the transition stage from dusty star-forming galaxies to passive populations, i.e. in the post-starburst phase. Another causal factor is the effect of the nuclear emission. AGN contribution would redden more rest-frame $V - J$ colours than $U - V$ colours, and thus this bias may rather weaken the colour discrepancy between HAEs and X-ray HAEs, though a more detailed analysis is needed.

3.3 Star-forming main sequence

We estimate the SFR$_{H\alpha}$ of HAEs from the observed Hα luminosities (Section 2.4.2) using the same method as Shimakawa et al. (2018). We use the Kennicutt (1998) prescription on the assumption of Chabrier (2003) IMF (a factor of 1.7 reduces SFR from the standard Kennicutt 1998 calibration). We then correct for dust extinction of the Hα line based on the SED-inferred stellar extinction (A_V) from the FAST code (Section 2.4.1) and the Calzetti et al. (2000) extinction
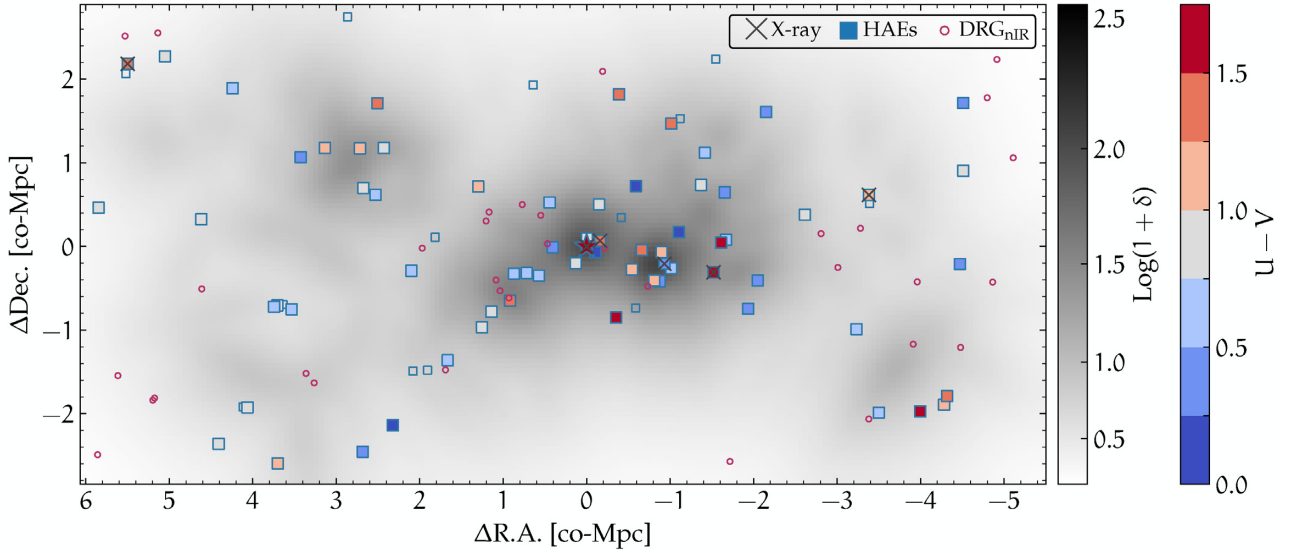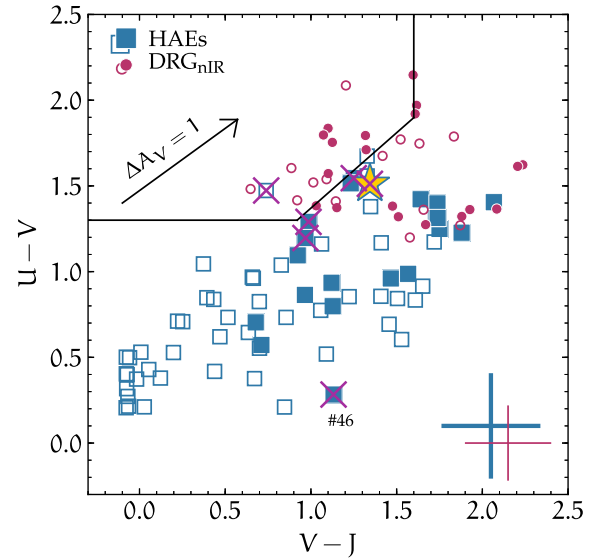
Figure 8. Spatial distribution with respect to the Spiderweb galaxy as shown by the star symbol in the centre. Large filled and small open squares are HAEs and HAE candidates, respectively. Symbol colours of HAEs indicate their rest-frame $U - V$ colours. Red circles and black crosses indicate DRG_{nIR} and X-ray sources, respectively. The colour map in the background shows the excess of surface number densities based on the 5th neighbour analysis.
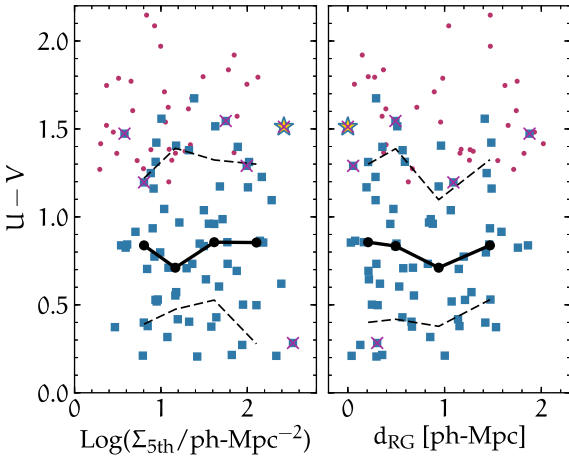
Figure 9. Rest-frame $U - V$ colours as a function of surface number densities of HAEs (from the left, Σ_{5th} ph-Mpc^{-2} and distance from the Spiderweb radio galaxy, d_{RG} ph-Mpc). The symbols are the same as in Fig. 7. Solid and dashed lines indicate median values and 68thpercentiles distributions of rest-frame $U - V$ colour of HAEs with respect to each axis.

Figure 10. Rest-frame *UVJ* colours of our HAE and DRG_{nIR} samples in the protocluster region. Blue squares and red circles are HAEs and DRG_{nIR}, respectively. Filled symbols indicate a $>2\sigma$ detection in either 3.6 or 4.5 μm, or both. We do not have sufficient IRAC photometry for open symbols, and those *VJ* colours are not reliable. Blue bold and red thin crosses on the lower right indicate typical errors of IRAC-detected HAEs and DRG_{nIR}, respectively. According to the EAZY code, the typical uncertainty of the objects without IRAC detections ($>2\sigma$) is $\sim$0.6 dex. The black arrow corresponds to the colour shift by dust reddening ($\Delta A_V = 1$) along the Calzetti et al. (2000) extinction law. The black solid line indicates the quiescent/star-forming classification line from Williams et al. (2009).

law. Throughout the analysis, we used the additional assumption of $E(B - V)_{\text{stellar}} = E(B - V)_{\text{nebular}}$. Such a hypothesis is relatively reasonable for typical star-forming galaxies at $z \sim 2$ (Reddy et al. 2015). However, Reddy et al. (2015) and Price et al. (2014) also note that the ratio of nebular extinction to stellar extinction depends on galaxy properties, especially SFR; our assumption, therefore, would lead to underestimating the SFRs of active and dusty star-forming objects. Previous infrared studies also suggest that the dust extinction law for individual galaxies varies depending on their IR luminosities and dust geometries (Reddy et al. 2006, 2010; Casey et al. 2014; Narayanan et al. 2018).

Indeed, we confirm that $SFR_{\text{UV + IR}}$ of dusty HAE sources with Spitzer/MIPS 24 μm detections is significantly higher than those dust-corrected $SFR_{\text{H}\alpha}$ with our tentative extinction correction (Fig. 11). Their IR luminosities are derived from the flux densities at

24 μm by following the Wuyts et al. (2008) conversion prescription and then obtaining their SFRs via $SFR_{\text{UV + IR}}$ ($= 1.09 \times 10^{-10}(L_{\text{IR}} + 3.3\nu L_{\nu, 2800})$, Bell et al. 2005). We only measure IR luminosities of 10 HAEs without X-ray detections (#5,9,13,14,22,27,61,71,80,93). Two of them (#27,93 but note #27 is blended with #26,29 in the MIPS/24 μm image) are associated with 870 μm LABOCA sources
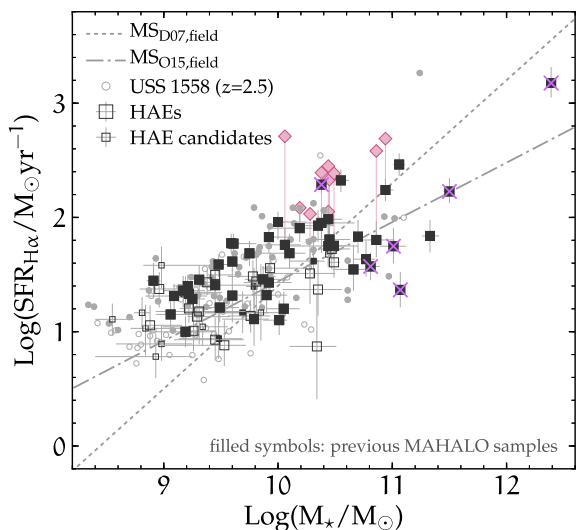
Figure 11. Stellar mass versus dust-corrected $SFR_{H\alpha}$ of HAEs. Black filled and open squares indicate HAEs and HAE candidates respectively (Table 2). The error-bars correspond to 1σ errors. Grey circles show HAEs in the USS 1558 protocluster at $z = 2.53$ reported by Shimakawa et al. (2018) which estimate $SFR_{H\alpha}$ in the same way. Purple crosses represent HAEs overlapping with the Chandra X-ray sources whose observed $H\alpha$ fluxes may be overestimated since we do not consider the flux contribution from AGNs. Grey dot-dashed and dashed lines are the star-forming main sequence of HAEs at $z = 2.2$ in the general field (Oteo et al. 2015) and star-forming galaxies at $z \sim 2$ reported by Daddi et al. (2007), respectively. Pink diamonds show SFRs derived from UV and IR luminosities for MIPS/24 µm detected HAEs (see text).

(DKB12 and DKB15 in Dannerbauer et al. 2014). According to the difference between dust-corrected $SFR_{H\alpha}$ and $SFR_{UV + IR}$, we expect to underestimate $SFR_{H\alpha}$ by a factor of four on average for these dusty HAEs. Such a large mismatch is the reason why we do not analyse the $H\alpha$ luminosity function in this paper, as discussed in the previous subsection.

The new deeper $H\alpha$ data succeed in finding relatively fainter HAEs than those found by the previous MAHALO-Subaru survey (Koyama et al. 2013a). As shown in Fig. 11, when we apply the same method for extinction correction of the $H\alpha$ line in HAEs in PKS 1138 as used for those in USS 1558 (Shimakawa et al. 2018), HAEs in PKS 1138 and USS 1558 seem to follow the same stellar mass – $SFR_{H\alpha}$ relation. We find no clear trend in star formation with environment, which is in agreement with past studies in the same field (Koyama et al. 2013a,b). However, finding no environmental dependence on star formation in PKS 1138 is in contrast to USS 1558 where the HAEs in the group regions are more actively star-forming than those in the intergroup regions (Shimakawa et al. 2018). Moreover, we find that three of the X-ray detected HAEs tend to be positioned below the main sequence, although these $SFR_{H\alpha}$ would be contaminated by additional $H\alpha$ emission from AGNs. This is consistent with their post-starburst like rest-*UVJ* colours (Section 3.2), though we should keep in mind that our dust corrections mass estimates of X-ray hosts have substantial uncertainties. One source showing the excess of star formation among HAEs with X-ray emission is HAE-#46 ($M_\star = 10^{10.4}$ $M_\odot$) that has a blue $U - V$ colour and Kurk et al. (2004b) have identified that this HAE (#215 in their literature) has a broad $H\alpha$ line.

Four HAEs (#42,48,54,56) are confirmed by ALMA CO(3 − 2) observations (Tadaki et al. in preparation). We cannot use these data

to derive their dust-corrected SFRs more robustly as they are clearly blended with other sources in the MIPS/24 µm band. However, #48,54 are more like dusty starbursts according to their rest-frame *UVJ* colours (Appendix C).

Our deeper $H\alpha$ imaging increases the number of HAE sources by 40–50 per cent compared to our previous narrow-band imaging (Koyama et al. 2013a). The mean narrow-band flux of newly identified HAEs is 2.5 times fainter than the mean flux of the entire sample. We discover eight HAEs at a stellar mass lower than 10^9 $M_\odot$ similar to those found in USS 1558 at $z = 2.5$ (Hayashi et al. 2016). The larger number of lower-mass HAEs in USS 1558 (Fig. 11) should be due to its 0.5 mag deeper K_s data than that in PKS 1138. We defer the detailed analyses of these samples to future work since it remains unclear whether they are truly HAEs associated with the PKS 1138 protocluster, due to a lack of firm detections at multi photometric bands. Future follow-up deep spectroscopy can provide us with both robust confirmations of these faint sources, and improved completeness when we investigate gas-phase metallicities of low-mass HAEs as compared to the previous spectroscopic analyses by Shimakawa et al. (2015).

3.4 The Spiderweb nebula

The previous $H\alpha$ line observations reported that the Spiderweb radio galaxy is associated with an extended $H\alpha$ nebula over a few ten ph-kpc in radius (Kurk et al. 2002; Nesvadba et al. 2006; Kuiper et al. 2011; Koyama et al. 2013a). Kurk et al. (2002) have derived Ly α/H α line ratios in different regions within the $H\alpha$ (Ly α) nebula. These vary between 0.015 (at the nucleus) and 7.6 (at the position blending with the radio jet). Nesvadba et al. (2006) have studied the spatial distribution and kinematics of the optical emission lines in detail by using the near-infrared integral field spectrograph (VLT/SPIFFI). Their emission line analyses suggest that the Spiderweb nebula has electron density $n_e \sim 388^{+182}_{-148}$ cm^{-3}, broad-line emission with FWHM>2000 km s^{-1}, typical [N II]/H α line flux ratio of $\sim$1, and the total observed $H\alpha$ luminosity of $L_{H\alpha} = (14.8 \pm 1.2) \times 10^{43}$ ergs s^{-1}. They roughly estimate the least total ionised gas mass of $M_{HII} = (2.3–6.5) \times 10^9$ $M_\odot$. Such a relatively high $H\alpha$ emission brightness cannot be explained by shock heating alone (Dopita & Sutherland 1996), so Nesvadba et al. (2006) conclude that photoionization from the radio galaxy plays a dominant role in the emission line properties of this large $H\alpha$ nebula (see also Villar-Martín et al. 2003; Nesvadba et al. 2008, 2017).

Our deep $H\alpha$ narrow-band imaging can trace extended $H\alpha$ (+ [N II]) emission over the wider FoV, down to 4.8×10^{-17} erg s^{-1} cm^{-2}arcsec^{-2} above the 1.5-sigma level in pixel scale. As a result, we succeed in identifying the large $H\alpha$ nebula structure that has a maximum projected extent of $\sim$100 ph-kpc (Fig. 12). Such an enormous $H\alpha$ structure has never been discovered before at $z > 2$. The $H\alpha$ nebula extends in the NE–SW direction, which is broadly consistent with the inclination of structures in X-ray and CO(1 − 0) emission found by Carilli et al. (2002) and Emonts et al. (2016), respectively.

When we adopt the conservative assumption of [N II]/H$\alpha = 1$ in the same manner as Nesvadba et al. (2006), we obtain the total observed H α luminosity $L_{H\alpha} = (1.35 \pm 0.15) \times 10^{44}$ ergs s^{-1} over 50 ph-kpc in radius. This value is consistent with the past result by Nesvadba et al. (2006). We should note that the obtained $H\alpha$ luminosity is a lower limit since dust correction is not implemented and the bandwidth of the narrow-band filter does not fully cover the broad-line emission as identified by Nesvadba et al. (2006). These complicated issues prevent us from exploring this unique nebula
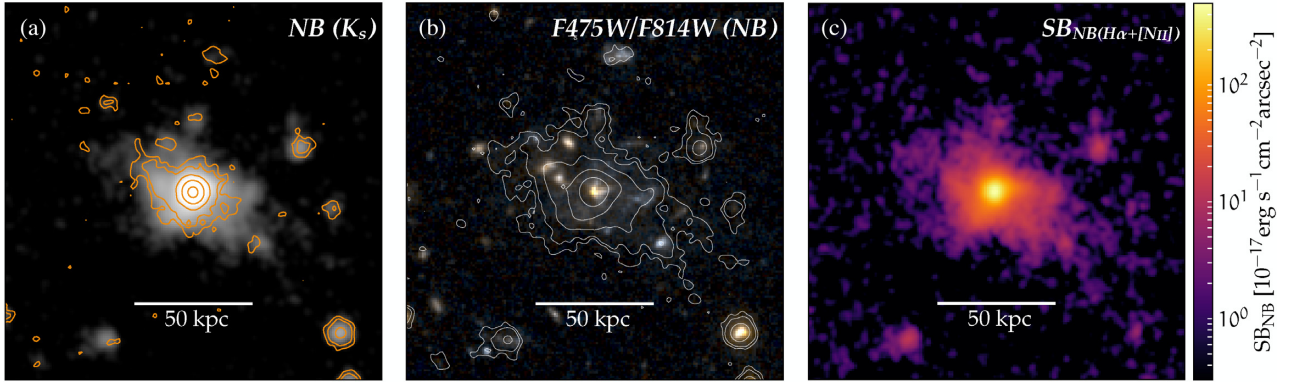
Figure 12. Multi-faces of the Spiderweb galaxy (20 arcsec on a side in each image). (a) The left-hand panel shows NB_{2071} image (grey scale) and line-subtracted K_s image (orange con tour). The first con tour is 1.5-sigma background rms. (b) The middle panel is an RGB image from F475W and F814W photometry with *HST*. White con tours are based on the NB_{2071} image, and the first con tour corresponds to 1.5 rms in the background. (c) The right-hand panel represents the surface brightness of narrow-band flux (SB_{NB}) where the continuum is subtracted (equation 3). 1-sigma error is 3.2×10^{-17} erg s^{-1} cm^{-2} arcsec^{-2} for a given pixel^2 area.
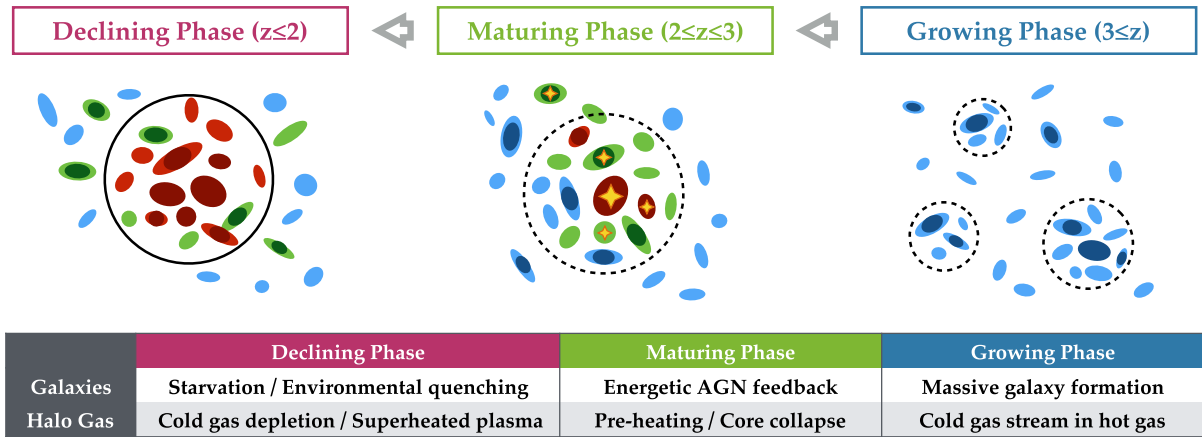
Figure 13. A speculative schematic of formation and evolution histories of galaxy clusters and galaxies therein, based on our findings through the MDCS. We tentatively assume that PKS 1138 at $z = 2.2$ is a maturing protocluster (middle) and USS 1558 at $z = 2.5$ is a growing protocluster (right), respectively, judging form substructures and characteristics of member galaxies. The left one represents the classical massive cluster of galaxies associated with a diffuse X-ray source. Galaxy colours are trying to express that the star formation declining and red sequence formation in the centre of galaxy clusters towards the local Universe. Yellow star symbols show energetic AGN activities. A table at the bottom highlights phenomena that are expected to occur in galaxies and (proto-)inter-cluster medium (see text).

in more detail. We experimentally carry out some further analyses with these caveats by comparing with *HST*/ACS images, which are shown in Appendix D.

Finally, we inspected the other HAEs in PKS 1138 searching for significantly extended H α structures based on the median stacking with the IRAF scripts. Our stacking procedure reaches down to 6.4×10^{-18} erg s^{-1} cm^{-2}arcsec^{-2} with a two-sigma confidence level. However, we do not identify such diffuse nebula beyond a radii of 10 ph-kpc in the other HAEs, even after stacking all HAE samples.

4 DISCUSSION

High-redshift protoclusters provide us with a great opportunity to unveil the formation histories of massive galaxy clusters and their member galaxies in the local Universe. As claimed by past studies (Kurk et al. 2004a; Kodama et al. 2007; Doherty et al. 2010; Hatch

et al. 2011; Galametz et al. 2012; Koyama et al. 2013a; Tanaka et al. 2013), PKS 1138 at $z = 2.2$ is considered to be one of the most massive protoclusters at $z \sim 2$, with a significant number excess ($\delta \gtrsim 10$) of massive red star-forming and passive galaxies over the MOIRCS FoV relative to the general field at a similar redshift. This suggests that the massive galaxies in PKS 1138 are in the maturing phase, and such red galaxies would provide us with direct insights into the quenching processes of bright red sequence objects seen in the present-day clusters of galaxies.

With such expectations, the original motivation of this work was to characterize these massive HAEs. We especially focus on X-ray fraction and the rest-frame *UVJ* colours of HAEs based on the Chandra X-ray data and multi-band images, both of which mostly cover the survey area. We first derive the stellar mass function and confirm the number excess of massive HAEs seen in the past studies (Hatch et al. 2011; Koyama et al. 2013a,b). The characteristic stellar mass is comparable to that in dense group cores seen in the USS

1558 protocluster (Shimakawa et al. 2018). However, PKS 1138 is associated with a larger number of massive red HAEs than USS 1558 (Kodama et al. 2007; Galametz et al. 2012), suggesting that PKS 1138 is a more developed system. In addition, considering the fact that the PKS 1138 protocluster hosts at least three passive galaxies in such a small field (Doherty et al. 2010; Tanaka et al. 2013, see also Zirm et al. 2008), PKS 1138 is ideally placed to see the rapid transition from massive dusty star-forming galaxies to quiescent galaxies.

We find that four out of the six very massive HAEs ($M_\star = 10^{11-12.5}$ M$_\odot$), including the Spiderweb galaxy, host bright X-ray sources ($L_X \gtrsim 10^{44}$ erg s^{-1}, see also Pentericci et al. 2002). In general fields at the similar redshift, Sobral et al. (2016) and Matthee et al. (2017) have shown that the AGN fraction significantly increases with increase in Hα luminosities of HAEs, and reaches ~100 per cent at the bright end ($>10^{43.5}$ erg s^{-1} without dust correction). Similarly, we confirm that the top two HAEs with high observed narrow-band luminosities ($=10^{43-43.5}$ erg s^{-1} without dust correction) and the Spiderweb radio galaxy ($=10^{44}$ erg s^{-1}) host X-ray counterparts. The fraction is about two times higher than those in general fields reported by them, although our sample size is quite small. Such a relatively fair comparison seems to strength our finding of the enhancement of AGN fraction in the protocluster region. Intriguingly, they tend to have unique rest-frame *UVJ* colours corresponding to the post-starburst sequence between star-forming galaxies and passive populations (Williams et al. 2009; Whitaker et al. 2011). Thus, AGNs may play an important role in suppressing the star formation and the build-up of massive quiescent galaxies since these massive HAEs are more likely to grow into the bright-end red sequence systems seen in the massive galaxy clusters in the local Universe. AGN feedback is indeed considered to be an important mechanism to suppress the star formation of massive systems as pointed out by previous work (e.g. Springel et al. 2005b; Croton et al. 2006; Bower et al. 2006; Somerville et al. 2008; van de Voort et al. 2011b; Page et al. 2012; Kormendy & Ho 2013; Cicone et al. 2014; Genzel et al. 2014). If a significant number of massive forming galaxies are subject to the influence of such strong feedback, we could explain the rapidly declining star formation around the distant cluster centres since $z \sim 2$ (Smail et al. 2014; Shimakawa et al. 2014; Clements et al. 2014; Kato et al. 2016).

We should note that the derived AGN fraction among HAEs is the minimum fraction inferred from the Chandra X-ray data. Our previous spectroscopic analyses (Shimakawa et al. 2015) indicate that other three sources (#14,30,54) might also be AGNs because of their high [N II]/Hα line ratios (>0.5), although the spectral data are obtained with low spectral resolution (R = 513) and the derived line ratios have substantial uncertainties (~0.2 dex). If we assume that these HAEs also host AGNs, the AGN fractions increase to 43 and 80 per cent at the stellar mass bins of $10^{10.5-11}$ and $10^{11-11.5}$ M$_\odot$ respectively. Such a large number of AGN host galaxies may affect the derivation of the stellar mass function, since their stellar mass estimates may be overestimated due to the flux contamination from the nuclear emission. In the meanwhile, the surprisingly high AGN fraction implies that massive star-forming galaxies in PKS 1138 may mostly host AGNs and could have a considerable impact on the current galaxy evolution paradigm.

The most energetic source present is the Spiderweb radio galaxy. We identified the enormous Hα structure extending over 100 ph-kpc associated with this massive system. The spatial extent broadly agrees with previous findings which have reported an extended component in the Lyα line (Gopal-Krishna & Wiita 2000; Kurk et al. 2002), X-ray (Carilli et al. 2002), UV (Pentericci et al. 1998;

Hatch et al. 2008), and the CO(1 − 0) line (Emonts et al. 2016). The Spiderweb galaxy is also known to be a composite of active star formation and AGN (Ogle et al. 2012; Drouart et al. 2014). The starburst component has SFR of ~1400 M$_\odot$ yr^{-1} (Seymour et al. 2012; Rawlings et al. 2013; Dannerbauer et al. 2014), supported by a rich gas reservoir of ~6×10^{10} M$_\odot$ (Emonts et al. 2013, 2016; Gullberg et al. 2016). This monster galaxy is expected to grow into a brightest cluster galaxy, as seen in the local Universe (Hatch et al. 2009). The large Hα nebula could show the occurrence of a pre-heating event in the proto-intercluster medium (Babul et al. 2002; Dubois et al. 2011, 2012; Valentino et al. 2016), though there is still much debate about heating mechanisms of the intercluster medium at high redshifts (McNamara & Nulsen 2007; Kravtsov & Borgani 2012).

Lastly, the very high X-ray fraction in massive HAEs cautions the possibility that the narrow-band HAE selection may overestimate an AGN fraction, especially at the massive end. For example, Sobral et al. (2016) have shown that AGNs typically contribute 15 per cent of the total H α luminosity. Moreover, AGNs are expected to enhance [N II] line flux (Baldwin, Phillips & Terlevich 1981; Veilleux & Osterbrock 1987) and this can additionally increase the narrow-band flux and EW$_{NB}$. For instance, for a given Hα luminosity, an increase of log [N II]/Hα ratio from −0.5 to 0 raises EW$_{NB}$ by 0.18 dex. These contaminations may cause the serious selection bias in the sense that the narrow-band selection preferentially detect AGN host HAEs. In particular, our current analyses cannot rule out the possibility that we are missing massive dusty starburst populations which would have faint observed Hα luminosities and low EW$_{NB}$ due to heavy dust obscuration. Even if we miss a few dust-obscured objects, this factor can substantially decrease the bright-end AGN fraction. A wide-field spectroscopic search at the IR to radio regime with e.g. ALMA and JWST is highly desirable to clarify this selection issue.

5 SUMMARY

In this second instalment of the MDCS campaign, we investigate HAEs associated with one of the most studied protoclusters, PKS 1138 at $z = 2.2$. Using the advanced data set we construct samples of HAEs associated with the Spiderweb protocluster; these consist of 68 HAEs (36 confirmed with spec-z and 32 selected by $Bz'K_s$ colour) and 13 HAE candidates. 17 and 9 objects amongst them are newly-discovered HAEs and HAE candidates by this work, respectively. The online catalogue (Appendix C) lists coordinates, confirmation status, physical properties, and rest-frame *UVJ* colours of the HAE samples. The major findings are summarized as follows.

–We investigate the stellar mass distribution function of HAEs in PKS 1138, including the completeness correction derived using a Monte Carlo simulation. We then identify the high cut-off stellar mass of log(M$_\star$/M$_\odot$) =11.73 ± 0.76 and find that the number density is about ten times higher over the survey area than that in the blank field. On the other hand, we find that at least four out of six very massive HAEs have X-ray counterparts, and those stellar masses may be significantly overestimated. This uncertainty would especially affect the derivation of the characteristic stellar mass. The Spiderweb nebula is unique and shows an extensive structure over 100 ph-kpc in the Hα emission line, as well as in other tracers such as Ly α, X-ray, UV, and CO(1 − 0) lines. We also tentatively obtain a passive fraction of 36 per cent by combining the HAE sample with DRG$_{nIR}$, although the measurement has a substantial error.

–We investigate the rest-frame *UVJ* colours of HAEs and their environmental dependence on the local scale. Given the limited survey field, we do not see any clear correlation between colours and local overdensities. On the other hand, HAEs with luminous X-ray emission tend to have post-starburst like colours, implying that bright AGNs may play an important role in quenching active star formation in these sources. Because the Spiderweb protocluster is also associated with a large number of dusty starbursts and passive galaxies, many massive galaxies in PKS 1138 seem to be undergoing a rapid transition from the active star formation phase into the quiescent mode.

Combined with our previous paper (Shimakawa et al. 2018), we here summarize the results that we obtained through the MDCS campaign. We have explored two protoclusters, USS 1558 ($z =$ 2.53) and PKS 1138 ($z = 2.15$) with the deep narrow-band imaging on the Subaru Telescope ($NB_{3\sigma} \sim 24$ mag).

The former target, USS 1558 is thought to be a young protocluster composed of fragmented dense groups as seen at higher redshifts (Umehata et al. 2015; Miller et al. 2018; Oteo et al. 2018). Shimakawa et al. (2018) have found that SFRs of HAEs in dense group cores are statistically higher than those in inter-group regions. Also, local overdensities show the higher cut-off stellar mass in the stellar mass function than the inter-group. These trends suggest that galaxy formation is more enhanced and accelerated in the fragmented groups in a growing phase of hierarchical growth of galaxy clusters (see also Wang et al. 2016; Oteo et al. 2018). Such an active star formation could be supported by a rich cold gas reservoir (Tadaki et al. in preparation) fed by vigorous cold accretion (e.g. Dekel & Birnboim 2006; Dekel et al. 2009a; Dekel, Sari & Ceverino 2009b; Kereš et al. 2009; Faucher-Giguère et al. 2010; van de Voort et al. 2011a). Another companion paper (Shimakawa et al. 2017) showing the Lyα photon depletion in the dense group regions could support this scenario.

PKS 1138 is thought to be a more advanced system because of the significant excess of bright red galaxies (Kurk et al. 2004a; Kodama et al. 2007; Doherty et al. 2010; Galametz et al. 2012). This work finds an enormous Hα structure associated with the Spiderweb radio galaxy and a high AGN fraction in massive HAEs. Such high-energy sources could contribute pre-heating in the proto-inter-cluster medium (Valentino et al. 2016), though heating mechanisms of inter-cluster medium in an early phase are highly uncertain observationally. Rest-frame *UVJ* colours of X-ray HAEs imply that they would be in a post-starburst phase, suggesting the importance of the role of AGN as a driver of star formation quenching. These results, together with previous work (Doherty et al. 2010; Tanaka et al. 2013; Koyama et al. 2013b), all point to PKS 1138 possibly being the sweet spot where maturing galaxies are undergoing a rapid transition from dusty starbursts to quenching populations.

At lower redshifts ($z \lesssim 2$), member galaxies in the hot inter-cluster medium enriched by superheated plasma would no longer retain their star formation because of insufficient gas accretion (Kereš et al. 2005; Sijacki et al. 2007; Schaye et al. 2010; McCarthy et al. 2011; Haines et al. 2013; Hughes et al. 2013; Jaffé et al. 2015, 2016; Bianconi, Marleau & Fadda 2016; Hayashi et al. 2017). Additionally, less massive galaxies falling into the clusters may experience environmental quenching as has previously been confirmed at $z <$ 2 (e.g. Bamford et al. 2009; Peng et al. 2010; Smith et al. 2012; Raichoor & Andreon 2012; Muzzin et al. 2012; Gobat et al. 2015; Brown et al. 2017).

Fig. 13 briefly summarizes these speculations based on the MDCS campaign. We strongly caution that the arguments discussed above are based on only two protoclusters and must therefore be viewed with caution. Future work is necessary to properly comprehend the systematic biases and appropriately understand the diversity of high-z protoclusters, as mentioned in the following section.

6 FUTURE PROSPECTS: DIVERSE PROTOCLUSTERS

Our MDCS program enables a high sampling density, down to a certain flux limit, with the deep narrow-band imaging: a unique advantage over the other common approaches such as photo-z and the Balmer/Lyman Break technique. On the other hand, we targeted only two known protoclusters at $z > 2$ which were initially discovered by surveys for radio galaxy environments (Kurk et al. 2000; Kajisawa et al. 2006). We thus should note that this work has not only a small sample size of protoclusters but also an unknown bias towards the environments associated with radio-loud galaxies. In particular, we do not yet know how the sampling effects affect the properties of member galaxies.

In recent years, many intensive protocluster-search survey projects have been launched. These utilize continuous strong absorption in the Lyα forest (Cai et al. 2016), Lyman Break features (Toshikawa et al. 2018), radio-loud galaxies (Noirot et al. 2018) and dust emission (Planck Collaboration XXVII 2015; Greenslade et al. 2018) as signposts. Whilst these surveys will each construct statistical protocluster catalogues, the sampling effects remain to be resolved. Future work will be needed to understand such selection biases and categorise individual protoclusters with, e.g. X-ray properties (Gobat et al. 2011; Valentino et al. 2016; Wang et al. 2016) and H I tomography (Lee et al. 2016). The upcoming eROSITA (Merloni et al. 2012), a successor to the ASTRO-H (Hitomi, Takahashi et al. 2016), and the Prime Focus Spectrograph on the Subaru Telescope (Tamura et al. 2016) will possess the exceptional capability needed to reveal these unique objects.

REFERENCES

Alexander D. M. et al., 2016, MNRAS, 461, 2944

Athreya R. M., Kapahi V. K., McCarthy P. J., van Breugel W., 1998, A&A, 329, 809

Babul A., Balogh M. L., Lewis G. F., Poole G. B., 2002, MNRAS, 330, 329

Baldwin J. A., Phillips M. M., Terlevich R., 1981, PASP, 93, 5

Bamford S. P. et al., 2009, MNRAS, 393, 1324

Barnes D. J. et al., 2017, MNRAS, 471, 1088

Bell E. F. et al., 2005, ApJ, 625, 23

Bertin E., Arnouts S., 1996, A&AS, 117, 393

Bianconi M., Marleau F. R., Fadda D., 2016, A&A, 588, A105

Blanton M. R., Moustakas J., 2009, ARA&A, 47, 159

Bolton J. G., Savage A., Wright A. E., 1979, Aust. J. Phys. Astrophys. Suppl., 46, 1

Bower R. G., Lucey J. R., Ellis R. S., 1992, MNRAS, 254, 601

Bower R. G., Kodama T., Terlevich A., 1998, MNRAS, 299, 1193

Bower R. G., Benson A. J., Malbon R., Helly J. C., Frenk C. S., Baugh C. M., Cole S., Lacey C. G., 2006, MNRAS, 370, 645

Brammer G. B., van Dokkum P. G., Coppi P., 2008, ApJ, 686, 1503

Brammer G. B. et al., 2011, ApJ, 739, 24

Brammer G. B. et al., 2012, ApJS, 200, 13

Brough S. et al., 2017, ApJ, 844, 59

Brown T. et al., 2017, MNRAS, 466, 1275

Bruzual G., Charlot S., 2003, MNRAS, 344, 1000

Bunker A. J., Warren S. J., Hewett P. C., Clements D. L., 1995, MNRAS, 273, 513

Butcher H., Oemler A., Jr, 1984, ApJ, 285, 426

Cai Z. et al., 2016, ApJ, 833, 135

Cai Z. et al., 2017, ApJ, 839, 131

Calabretta M. R., Greisen E. W., 2002, A&A, 395, 1077

Calzetti D., Armus L., Bohlin R. C., Kinney A. L., Koornneef J., Storchi-Bergmann T., 2000, ApJ, 533, 682

Capak P. et al., 2007, ApJS, 172, 99

Cappellari M. et al., 2011, MNRAS, 416, 1680

Carilli C. L., Röttgering H. J. A., van Ojik R., Miley G. K., van Breugel W. J. M., 1997, ApJS, 109, 1

Carilli C. L., Harris D. E., Pentericci L., Röttgering H. J. A., Miley G. K., Kurk J. D., van Breugel W., 2002, ApJ, 567, 781

Casey C. M. et al., 2014, ApJ, 796, 95

Chabrier G., 2003, PASP, 115, 763

Chiang Y.-K., Overzier R., Gebhardt K., 2013, ApJ, 779, 127

Chiang Y.-K., Overzier R. A., Gebhardt K., Henriques B., 2017, ApJ, 844, L23

Cicone C. et al., 2014, A&A, 562, A21

Clements D. L. et al., 2014, MNRAS, 439, 1193

Couch W. J., Barger A. J., Smail I., Ellis R. S., Sharples R. M., 1998, ApJ, 497, 188

Croft S., Kurk J., van Breugel W., Stanford S. A., de Vries W., Pentericci L., Röttgering H., 2005, AJ, 130, 867

Croton D. J. et al., 2006, MNRAS, 365, 11

Daddi E., Cimatti A., Renzini A., Fontana A., Mignoli M., Pozzetti L., Tozzi P., Zamorani G., 2004, ApJ, 617, 746

Daddi E. et al., 2005, ApJ, 626, 680

Daddi E. et al., 2007, ApJ, 670, 156

Dannerbauer H. et al., 2014, A&A, 570, A55

Dannerbauer H. et al., 2017, A&A, 608, A48

Darvish B., Mobasher B., Sobral D., Rettura A., Scoville N., Faisst A., Capak P., 2016, ApJ, 825, 113

Davidzon I. et al., 2017, A&A, 605, A70

de Vaucouleurs G., 1961, ApJS, 5, 233

Dekel A., Birnboim Y., 2006, MNRAS, 368, 2

Dekel A. et al., 2009a, Nature, 457, 451

Dekel A., Sari R., Ceverino D., 2009b, ApJ, 703, 785

Di Matteo T., Springel V., Hernquist L., 2005, Nature, 433, 604

Doherty M. et al., 2010, A&A, 509, A83

Dopita M. A., Sutherland R. S., 1996, ApJS, 102, 161

Dressler A., 1980, ApJ, 236, 351

Dressler A. et al., 1997, ApJ, 490, 577

Drouart G. et al., 2014, A&A, 566, A53

Dubois Y., Devriendt J., Teyssier R., Slyz A., 2011, MNRAS, 417, 1853

Dubois Y., Devriendt J., Slyz A., Teyssier R., 2012, MNRAS, 420, 2662

Elsner F., Feulner G., Hopp U., 2008, A&A, 477, 503

Emonts B. H. C. et al., 2013, MNRAS, 430, 3465

Emonts B. H. C. et al., 2016, Science, 354, 1128

Emonts B. H. C. et al., 2018, MNRAS, 477, L60

Evans I. N. et al., 2010, ApJS, 189, 37

Fabjan D., Borgani S., Tornatore L., Saro A., Murante G., Dolag K., 2010, MNRAS, 401, 1670

Fang J. J. et al., 2018, ApJ, 858, 100

Faucher-Giguère C.-A., Kereš D., Dijkstra M., Hernquist L., Zaldarriaga M., 2010, ApJ, 725, 633

Ferrarese L., Merritt D., 2000, ApJ, 539, L9

Fitzpatrick E. L., 1999, PASP, 111, 63

Fogarty L. M. R. et al., 2014, MNRAS, 443, 485

Franx M. et al., 2003, ApJ, 587, L79

Galametz A. et al., 2012, ApJ, 749, 169

Geach J. E., Smail I., Best P. N., Kurk J., Casali M., Ivison R. J., Coppin K., 2008, MNRAS, 388, 1473

Genzel R. et al., 2014, ApJ, 796, 7

Gobat R. et al., 2011, A&A, 526, A133

Gobat R. et al., 2015, A&A, 581, A56

Gopal-Krishna Wiita P. J., 2000, ApJ, 529, 189

Goto T. et al., 2003, PASJ, 55, 739

Greenslade J. et al., 2018, MNRAS, 476, 3336

Greisen E. W., Calabretta M. R., 2002, A&A, 395, 1061

Grogin N. A. et al., 2011, ApJS, 197, 35

Gullberg B. et al., 2016, A&A, 591, A73

Haines C. P. et al., 2013, ApJ, 775, 126

Hatch N. A., Overzier R. A., Röttgering H. J. A., Kurk J. D., Miley G. K., 2008, MNRAS, 383, 931

Hatch N. A., Overzier R. A., Kurk J. D., Miley G. K., Röttgering H. J. A., Zirm A. W., 2009, MNRAS, 395, 114

Hatch N. A., Kurk J. D., Pentericci L., Venemans B. P., Kuiper E., Miley G. K., Röttgering H. J. A., 2011, MNRAS, 415, 2993

Hatch N. A. et al., 2014, MNRAS, 445, 280

Hayashi M., Kodama T., Koyama Y., Tanaka I., Shimasaku K., Okamura S., 2010, MNRAS, 402, 1980

Hayashi M., Kodama T., Tadaki K.-i., Koyama Y., Tanaka I., 2012, ApJ, 757, 15

Hayashi M., Kodama T., Tanaka I., Shimakawa R., Koyama Y., Tadaki K.-i., Suzuki T. L., Yamamoto M., 2016, ApJ, 826, L28

Hayashi M. et al., 2017, ApJ, 841, L21

Hayashi M. et al., 2018a, PASJ, 70, S17

Hayashi M. et al., 2018b, ApJ, 856, 118

Hayward C. C., Kereš D., Jonsson P., Narayanan D., Cox T. J., Hernquist L., 2011, ApJ, 743, 159

Hennawi J. F., Prochaska J. X., Cantalupo S., Arrigoni-Battaia F., 2015, Science, 348, 779

Hopkins P. F., Cox T. J., Younger J. D., Hernquist L., 2009, ApJ, 691, 1168

Hopkins P. F., Cox T. J., Hernquist L., Narayanan D., Hayward C. C., Murray N., 2013, MNRAS, 430, 1901

Houghton R. C. W. et al., 2013, MNRAS, 436, 19

Hughes T. M., Cortese L., Boselli A., Gavazzi G., Davies J. I., 2013, A&A, 550, A115

Ichikawa T. et al., 2006, Proc. SPIE, 6269, 626916

Ilbert O. et al., 2013, A&A, 556, A55

Jaffé Y. L., Smith R., Candlish G. N., Poggianti B. M., Sheen Y.-K., Verheijen M. A. W., 2015, MNRAS, 448, 1715

Jaffé Y. L. et al., 2016, MNRAS, 461, 1202

Kajisawa M., Kodama T., Tanaka I., Yamada T., Bower R., 2006, MNRAS, 371, 577

Kato Y. et al., 2016, MNRAS, 460, 3861

Kauffmann G. et al., 2003, MNRAS, 346, 1055

Kauffmann G., White S. D. M., Heckman T. M., Ménard B., Brinchmann J., Charlot S., Tremonti C., Brinkmann J., 2004, MNRAS, 353, 713

Kennicutt R. C., Jr, 1998, ARA&A, 36, 189

Kereš D., Katz N., Weinberg D. H., Davé R., 2005, MNRAS, 363, 2

Kereš D., Katz N., Davé R., Fardal M., Weinberg D. H., 2009, MNRAS, 396, 2332

Kodama T., Bower R. G., 2001, MNRAS, 321, 18

Kodama T., Tanaka I., Kajisawa M., Kurk J., Venemans B., De Breuck C., Vernet J., Lidman C., 2007, MNRAS, 377, 1717

Kodama T., Hayashi M., Koyama Y., Tadaki K.-i., Tanaka I., Shimakawa R., 2013, in Thomas D., Pasquali A., Ferreras I., eds, Proc. IAU Symposium Vol. 295, The Intriguing Life of Massive Galaxies. Cambridge Univ. Press, Cambridge, p. 74

Koekemoer A. M. et al., 2011, ApJS, 197, 36

Kormendy J., Ho L. C., 2013, ARA&A, 51, 511

Koyama Y., Kodama T., Shimasaku K., Hayashi M., Okamura S., Tanaka I., Tokoku C., 2010, MNRAS, 403, 1611

Koyama Y., Kodama T., Nakata F., Shimasaku K., Okamura S., 2011, ApJ, 734, 66

Koyama Y., Kodama T., Tadaki K.-i., Hayashi M., Tanaka M., Smail I., Tanaka I., Kurk J., 2013a, MNRAS, 428, 1551

Koyama Y. et al., 2013b, MNRAS, 434, 423

Kravtsov A. V., Borgani S., 2012, ARA&A, 50, 353

Kriek M., van Dokkum P. G., Labbé I., Franx M., Illingworth G. D., Marchesini D., Quadri R. F., 2009, ApJ, 700, 221

Kriek M. et al., 2015, ApJS, 218, 15

Krishnan C. et al., 2017, MNRAS, 470, 2170

Kubo M. et al., 2013, ApJ, 778, 170

Kubo M., Yamada T., Ichikawa T., Kajisawa M., Matsuda Y., Tanaka I., Umehata H., 2017, MNRAS, 469, 2235

Kuiper E. et al., 2011, MNRAS, 415, 2245

Kurk J. D. et al., 2000, A&A, 358, L1

Kurk J. D., Pentericci L., Röttgering H. J. A., Miley G. K., 2002, Rev. Mex. Astron. Astrofis. Ser. Conf., 13, 191

Kurk J., Röttgering H., Pentericci L., Miley G., Overzier R., 2003, New Astron. Rev., 47, 339

Kurk J. D., Pentericci L., Röttgering H. J. A., Miley G. K., 2004a, A&A, 428, 793

Kurk J. D., Pentericci L., Overzier R. A., Röttgering H. J. A., Miley G. K., 2004b, A&A, 428, 817

Laigle C. et al., 2016, ApJS, 224, 24

Lasker B. M. et al., 2008, AJ, 136, 735

Lee K.-G. et al., 2016, ApJ, 817, 160

Lehmer B. D. et al., 2009, ApJ, 691, 687

Lehmer B. D. et al., 2013, ApJ, 765, 87

Lopes P. A. A., Ribeiro A. L. B., Rembold S. B., 2017, MNRAS, 472, 409

Lovell C. C., Thomas P. A., Wilkins S. M., 2018, MNRAS, 474, 4612

Macuga M. et al., 2018, preprint (arXiv:1805.06569)

Mannucci F., Cresci G., Maiolino R., Marconi A., Gnerucci A., 2010, MNRAS, 408, 2115

Markwardt C. B., 2009, in Bohlender D. A., Durand D., Dowler P., eds, ASP Conf. Ser. Vol. 411, Astronomical Data Analysis Software and Systems XVIII. Astron. Soc. Pac., San Francisco, p. 251

Matthee J., Sobral D., Best P., Smail I., Bian F., Darvish B., Röttgering H., Fan X., 2017, MNRAS, 471, 629

Mayo J. H., Vernet J., De Breuck C., Galametz A., Seymour N., Stern D., 2012, A&A, 539, A33

McCarthy I. G. et al., 2010, MNRAS, 406, 822

McCarthy I. G., Schaye J., Bower R. G., Ponman T. J., Booth C. M., Dalla Vecchia C., Springel V., 2011, MNRAS, 412, 1965

McCracken H. J. et al., 2012, A&A, 544, A156

McNamara B. R., Nulsen P. E. J., 2007, ARA&A, 45, 117

Mei S. et al., 2009, ApJ, 690, 42

Merloni A. et al., 2010, ApJ, 708, 137

Merloni A. et al., 2012, preprint (arXiv:1209.3114)

Miley G. K. et al., 2006, ApJ, 650, L29

Miller T. B. et al., 2018, Nature, 556, 469

Moresco M. et al., 2013, A&A, 558, A61

Muzzin A., Marchesini D., van Dokkum P. G., Labbé I., Kriek M., Franx M., 2009, ApJ, 701, 1839

Muzzin A. et al., 2012, ApJ, 746, 188

Muzzin A. et al., 2013, ApJ, 777, 18

Narayanan D. et al., 2015, Nature, 525, 496

Narayanan D., Davé R., Johnson B. D., Thompson R., Conroy C., Geach J., 2018, MNRAS, 474, 1718

Nesvadba N. P. H., Lehnert M. D., Eisenhauer F., Gilbert A., Tecza M., Abuter R., 2006, ApJ, 650, 693

Nesvadba N. P. H., Lehnert M. D., De Breuck C., Gilbert A. M., van Breugel W., 2008, A&A, 491, 407

Nesvadba N. P. H., Drouart G., De Breuck C., Best P., Seymour N., Vernet J., 2017, A&A, 600, A121

Noble A. G. et al., 2017, ApJ, 842, L21

Noirot G. et al., 2018, ApJ, 859, 38

Ogle P., Davies J. E., Appleton P. N., Bertincourt B., Seymour N., Helou G., 2012, ApJ, 751, 13

Oke J. B., Gunn J. E., 1983, ApJ, 266, 713

Osterbrock D. E., 1974, Astrophysics of Gaseous Nebulae. W. H. Freeman & Co., San Francisco

Oteo I., Sobral D., Ivison R. J., Smail I., Best P. N., Cepa J., Pérez-García A. M., 2015, MNRAS, 452, 2018

Oteo I. et al., 2018, ApJ, 856, 72

Page M. J. et al., 2012, Nature, 485, 213

Paulino-Afonso A., Sobral D., Darvish B., Ribeiro B., Stroe A., Best P., Afonso J., Matsuda Y., 2018, preprint (arXiv:1805.07371)

Peebles P. J. E., 1970, AJ, 75, 13

Peng Y.-j. et al., 2010, ApJ, 721, 193

Pentericci L., Roettgering H. J. A., Miley G. K., Carilli C. L., McCarthy P., 1997, A&A, 326, 580

Pentericci L., Röttgering H. J. A., Miley G. K., Spinrad H., McCarthy P. J., van Breugel W. J. M., Macchetto F., 1998, ApJ, 504, 139

Pentericci L. et al., 2000, A&A, 361, L25

Pentericci L., Kurk J. D., Carilli C. L., Harris D. E., Miley G. K., Röttgering H. J. A., 2002, A&A, 396, 109

Pettini M., Pagel B. E. J., 2004, MNRAS, 348, L59

Planck CollaborationXXVII, 2015, A&A, 582, A30

Price S. H. et al., 2014, ApJ, 788, 86

Raichoor A., Andreon S., 2012, A&A, 543, A19

Rawlings J. I. et al., 2013, MNRAS, 429, 744

Reddy N. A., Steidel C. C., Fadda D., Yan L., Pettini M., Shapley A. E., Erb D. K., Adelberger K. L., 2006, ApJ, 644, 792

Reddy N. A., Erb D. K., Pettini M., Steidel C. C., Shapley A. E., 2010, ApJ, 712, 1070

Reddy N. A. et al., 2015, ApJ, 806, 259

Rieke G. H. et al., 2015, PASP, 127, 584

Rigby E. E. et al., 2014, MNRAS, 437, 1882

Roettgering H. J. A., Lacy M., Miley G. K., Chambers K. C., Saunders R., 1994, A&AS, 108, 79

Roettgering H. J. A., van Ojik R., Miley G. K., Chambers K. C., van Breugel W. J. M., de Koff S., 1997, A&A, 326, 505

Romeo A. D., Kang X., Contini E., Sommer-Larsen J., Fassbender R., Napolitano N. R., Antonuccio-Delogu V., Gavignaud I., 2015, A&A, 581, A50

Röttgering H., Daddi E., Overzier R., Wilman R., 2003, New Astron. Rev., 47, 309

Santini P. et al., 2012, A&A, 540, A109

Schaye J. et al., 2010, MNRAS, 402, 1536

Schechter P., 1976, ApJ, 203, 297

Schlafly E. F., Finkbeiner D. P., 2011, ApJ, 737, 103

Schlegel D. J., Finkbeiner D. P., Davis M., 1998, ApJ, 500, 525

Scoville N. et al., 2007, ApJS, 172, 1

Seymour N. et al., 2007, ApJS, 171, 353

Seymour N. et al., 2012, ApJ, 755, 146

Shimakawa R., Kodama T., Tadaki K.-i., Tanaka I., Hayashi M., Koyama Y., 2014, MNRAS, 441, L1

Shimakawa R., Kodama T., Tadaki K.-i., Hayashi M., Koyama Y., Tanaka I., 2015, MNRAS, 448, 666

Shimakawa R. et al., 2017, MNRAS, 468, L21

Shimakawa R. et al., 2018, MNRAS, 473, 1977

Sijacki D., Springel V., Di Matteo T., Hernquist L., 2007, MNRAS, 380, 877

Skelton R. E. et al., 2014, ApJS, 214, 24

Smail I. et al., 2014, ApJ, 782, 19

Smith R. J., Lucey J. R., Price J., Hudson M. J., Phillipps S., 2012, MNRAS, 419, 3167

Sobral D. et al., 2009, MNRAS, 398, 75

Sobral D., Best P. N., Matsuda Y., Smail I., Geach J. E., Cirasuolo M., 2012, MNRAS, 420, 1926

Sobral D., Smail I., Best P. N., Geach J. E., Matsuda Y., Stott J. P., Cirasuolo M., Kurk J., 2013, MNRAS, 428, 1128

Sobral D., Best P. N., Smail I., Mobasher B., Stott J., Nisbet D., 2014, MNRAS, 437, 3516

Sobral D., Kohn S. A., Best P. N., Smail I., Harrison C. M., Stott J., Calhau J., Matthee J., 2016, MNRAS, 457, 1739

Somerville R. S., Hopkins P. F., Cox T. J., Robertson B. E., Hernquist L., 2008, MNRAS, 391, 481

Springel V., Di Matteo T., Hernquist L., 2005a, MNRAS, 361, 776

Springel V. et al., 2005b, Nature, 435, 629

Steidel C. C., Adelberger K. L., Dickinson M., Giavalisco M., Pettini M., Kellogg M., 1998, ApJ, 492, 428

Steidel C. C., Adelberger K. L., Shapley A. E., Pettini M., Dickinson M., Giavalisco M., 2000, ApJ, 532, 170

Steidel C. C., Adelberger K. L., Shapley A. E., Erb D. K., Reddy N. A., Pettini M., 2005, ApJ, 626, 44

Steidel C. C. et al., 2014, ApJ, 795, 165

Stevens J. A. et al., 2003, Nature, 425, 264

Straatman C. M. S. et al., 2016, ApJ, 830, 51

Sunyaev R. A., Zeldovich Y. B., 1972, A&A, 20, 189

Suzuki R. et al., 2008, PASJ, 60, 1347

Tadaki K.-i. et al., 2012, MNRAS, 423, 2617

Tadaki K.-i., Kodama T., Tanaka I., Hayashi M., Koyama Y., Shimakawa R., 2013, ApJ, 778, 114

Tadaki K.-i. et al., 2015, ApJ, 811, L3

Takahashi T. et al., 2016, Proc. SPIE, 9905, 99050U

Tamura N. et al., 2016, Proc. SPIE, 9908, 99081M

Tanaka M., Kodama T., Arimoto N., Okamura S., Umetsu K., Shimasaku K., Tanaka I., Yamada T., 2005, MNRAS, 362, 268

Tanaka M., De Breuck C., Venemans B., Kurk J., 2010, A&A, 518, A18

Tanaka I. et al., 2011, PASJ, 63, 415

Tanaka M. et al., 2013, ApJ, 772, 113

Taniguchi Y. et al., 2007, ApJS, 172, 9

Taylor M. B., 2015, in Taylor A. R., Rosolowsky E., eds, ASP Conf. Ser. Vol. 495, Astronomical Society of the Pacific Conference Series. Astron. Soc. Pac., San Francisco, p. 177

Taylor G. B., Barton E. J., Ge J., 1994, AJ, 107, 1942

Terlevich A. I., Caldwell N., Bower R. G., 2001, MNRAS, 326, 1547

Tody D., 1993, in Hanisch R. J., Brissenden R. J. V., Barnes J., eds, Astronomical Data Analysis Software and Systems II, ASP Conf. Ser. Vol. 52, IRAF in the Nineties. Astron. Soc. Pac., San Francisco, p. 173

Toshikawa J. et al., 2018, PASJ, 70, S12

Tremonti C. A. et al., 2004, ApJ, 613, 898

Umehata H. et al., 2015, ApJ, 815, L8

Valentino F. et al., 2016, ApJ, 829, 53

Valtchanov I. et al., 2013, MNRAS, 436, 2505

van Albada G. B., 1961, AJ, 66, 590

van de Voort F., Schaye J., Booth C. M., Haas M. R., Dalla Vecchia C., 2011a, MNRAS, 414, 2458

van de Voort F., Schaye J., Booth C. M., Dalla Vecchia C., 2011b, MNRAS, 415, 2782

van der Burg R. F. J. et al., 2013, A&A, 557, A15

van der Wel A., 2008, ApJ, 675, L13

van Dokkum P. G. et al., 2004, ApJ, 611, 703

Veilleux S., Osterbrock D. E., 1987, ApJS, 63, 295

Venemans B. P. et al., 2007, A&A, 461, 823

Villar-Martín M., Vernet J., di Serego Alighieri S., Fosbury R., Humphrey A., Pentericci L., 2003, MNRAS, 346, 273

Visvanathan N., Sandage A., 1977, ApJ, 216, 214

Wang T. et al., 2016, ApJ, 828, 56

Wetzel A. R., Tinker J. L., Conroy C., 2012, MNRAS, 424, 232

Whitaker K. E. et al., 2011, ApJ, 735, 86

Williams R. J., Quadri R. F., Franx M., van Dokkum P., Labbé I., 2009, ApJ, 691, 1879

Wuyts S., Labbé I., Förster Schreiber N. M., Franx M., Rudnick G., Brammer G. B., van Dokkum P. G., 2008, ApJ, 682, 985

Zirm A. W. et al., 2008, ApJ, 680, 224

SUPPORTING INFORMATION

Supplementary data are available at *MNRAS* online.

Table C1. Catalogue columns.

Please note: Oxford University Press is not responsible for the content or functionality of any supporting materials supplied by the authors. Any queries (other than missing material) should be directed to the corresponding author for the article.

APPENDIX A: COLOUR-TERM EFFECT

We measured colour term variations ($K_s - NB_{2071}$) of individual galaxies, which are caused by the slight margin of filter wavelength between narrow-band (NB_{2071}) and broad-band (K_s) filters. Deriving the typical colour term is important not only to minimize the systematic error of derived narrow-band fluxes and EWs of HAEs but also to determine the reasonable EW threshold free of the contaminants from non-emitters.

We show three examples of the colour term distribution across the redshift range between 0 and 4 based on SEDs of single stellar population (SSP) synthesis models (Bruzual & Charlot 2003) with ages of 0.1, 0.9, and 2.5 Gyr (Fig. A1). We fix the stellar metallicity to $Z = 0.008$ and apply two different extinctions ($A_V = 0$ and 1). It is easy to identify that the colour term decreases with increasing redshift, especially for older (i.e. redder) SED models. One should note that other models with different star formation histories or initial parameters do not significantly deviate from the range covered by these examples except when we employ extremely obscured (reddened) objects.

Also, we demonstrated the colour terms of photo-z sources from the 3D-*HST* library (Skelton et al. 2014) and obtained HAE samples whose SED spectra are based on the FAST SED-fitting code (Kriek et al. 2009). We employ the same initial parameters in the SED-fitting for both samples (Section 2.4.1). The inferred colour term variations can be found in Fig. A1. We derived the colour term variation (68th percentile) of -0.02 ± 0.06 in photo-z sources at
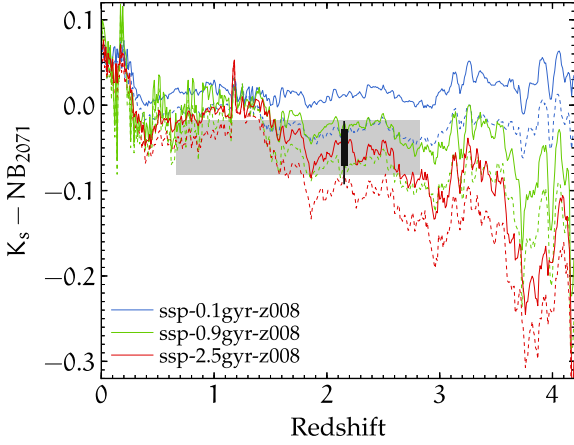
Figure A1. Colour-term distribution of $K_s - NB_{2071}$ as a function of redshift in SSP models (Bruzual & Charlot 2003) with three different ages (from the top, 0.1 Gyr: *blue*, 0.9 Gyr: *green*, and 2.5 Gyr: *red*). Solid and dashed curves indicate zero extinction, and $A_V = 1$, respectively. The metallicities are fixed to $Z = 0.008$ in each model. The grey-shaded region is the 68th percentile distribution inferred from SEDs of photo-z sources at $K_s = 21$–23 mag based on the 3D-*HST* photometry catalogue (Skelton et al. 2014). Black thick and thin vertical lines indicate 68th and 95th percentiles of the colour-term distributions of HAEs estimated from the model-inferred SEDs with the FAST code (Section 2.4.1).

$K_s = 21$–23 mag that is comparable with K_s-band magnitudes of most HAE samples (Fig. 2). This colour term variation almost corresponds to the 95th percentile distribution for the entire HAE samples. As mentioned in Section 2.3, we decide to use the fixed colour term value of $K_s - NB_{2071} = -0.04$ since <0.1 mag scatter of the colour term effect is negligibly small relative to the total error in the narrow-band flux.

APPENDIX B: SAMPLE COMPLETENESS

Evaluating the completeness of narrow-band emitters requires an additional correction for the narrow-band selection process on top of the detection completeness. This work estimates the completeness as a function of narrow-band magnitude based on a Monte Carlo simulation in the same way as in Shimakawa et al. (2018). We first embedded 10 PSF sources at the narrow-band magnitude of 19–25 mag, in steps of 0.2 mag, into the reduced NB_{2071} and K_s-band images. The PSF model is made by median stacking 32 bright point sources in the survey area. We should note that embedded PSFs at NB_{2071} band implement line fluxes and the colour term dispersion in each PSF. The inserted narrow-band flux is determined by the PSF's narrow-band magnitude (Fig. B1). Also, the colour term variation ($K_s - NB_{2071} = -0.02 \pm 0.06$) is derived from the result in the previous section. After that, we estimate the recovery rate in the detection process (i.e. detection completeness) and colour selection process (i.e. selection completeness) based on photometry with SExtractor (version 2.19.5; Bertin & Arnouts 1996). In the latter case, we calculated the recovery rate for sources that satisfy the criteria for the narrow-band excess (equation 1 and equation 2). This test was repeated 50 times for a given magnitude, and thus we simulated the total 500 PSF sources at each magnitude range.

The obtained detection and selection completeness are indicated in Fig. B1. We fit the resultant completeness fraction by a comple-
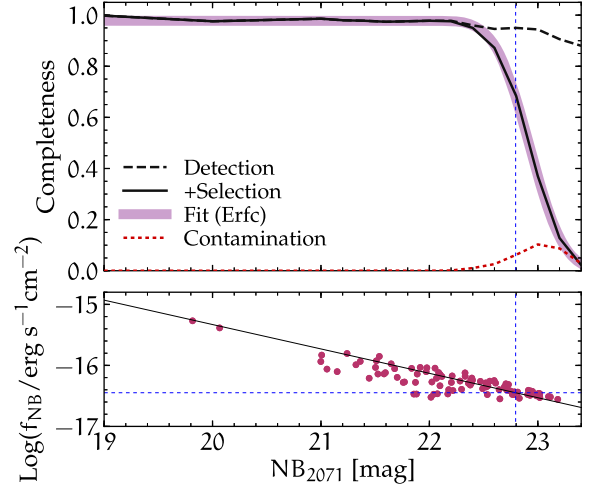
Figure B1. Sample completeness as a function of narrow-band magnitude. Dashed and solid lines indicate the detection completeness and the completeness incorporating the selection process as well. We fitted the recovery rate by a complementary error function as shown by the thick purple curve. The red dotted line is the contamination rate. In the lower panel, red dots represent log narrowband fluxes (f_{NB}) across the narrow-band magnitude for the narrow-band emitters. In our simulation, we fix the embedded line flux into the narrow-band image by the narrow-band magnitude of PSFs along the regression line shown by the solid black line. The blue vertical and perpendicular lines indicate 68 per cent completeness.

mentary error function (Erfc(x)),

$$C(NB) = 0.489 \times \text{Erfc}(2.827 \times (NB - 22.923)), \quad \text{(B1)}$$

which provides a better solution than polynomial and arctangent functions. $C(NB)^{-1}$ is the completeness correction factor that we applied to the derivation of the distribution function in Section 3.1. According to our simulation, the 68 per cent completeness limit corresponds to a narrow-band magnitude of 22.80. One should note that narrow-band emitters with lower line fluxes should possess lower completeness for a given narrow-band magnitude. This factor could lead to a systematic error in the analyses of the distribution functions (Section 3.1) at the faint end. We stress that such an error can be ignored as we remove faint-end sources for the curve fitting when we derive the distribution functions.

This work also estimates the contamination rate caused by the combined effects of the photometric errors and the colour term. To do so, we run the same simulation without adding line flux to the narrow-band sources, and then calculate the contaminants showing flux excess at NB_{2071} relative to K_s-band. We then confirm that our selection criteria (equation 1 and equation 2) ignores such contaminations at $NB_{2071} < 22.4$ mag. On the other hand, the simulation suggests a 5–10 per cent contamination rate at the faint end. However, we do not consider this uncertainty since faint sources are outside the scope of this paper.

APPENDIX C: EMITTER CATALOGUE

The HAE catalogue is available as the online material. Descriptions about each column can be found in Table C1. One should note that the $SFR_{H\alpha, \text{corr}}$ error (eSFR_Ha) would have additional uncertainties due to the systematic errors of dust extinction correction (see Section 3.3), though the errors of model-inferred A_V are included.

Table C1. Catalogue columns. A full version of this table is available online.

Name	Description
ID	Identification number
RA	RA J2000 [degree]
Dec	DEC J2000 [degree]
z	Spectroscopic redshift
z_flag	*Spec-z reference (id)
Ms	Log stellar mass [$M_\odot$]
Ms_el	Lower 1σ error of Ms
Ms_eu	Upper 1σ error of Ms
Av	Amount of dust extinction at V-band
Av_el	Lower 1σ error of Av
Av_eu	Upper 1σ error of Av
LHa	Observed H α luminosity [erg s^{-1}]
LHa_e	1σ error of $L_{H\alpha}$ [erg s^{-1}]
SFR	Dust-corrected log SFR$_{H\alpha}$ [$M_\odot$ yr^{-1}]
SFR_el	Lower 1σ error of SFR [$M_\odot$ yr^{-1}]
SFR_eu	Upper 1σ error of SFR [$M_\odot$ yr^{-1}]
UV	Rest-frame ($U - V$) colour
VJ	Rest-frame ($V - J$) colour
X_flag	X-ray counterpart (id in Pentericci et al. 2002)
LAE	Ly α emitter counterpart (id in Kurk et al. 2004a)

Note. *P02: Pentericci et al. (2002), K04: Kurk et al. (2004b)
C05: Croft et al. (2005), D10: Doherty et al. (2010)
T13: Tanaka et al. (2013), S14: Shimakawa et al. (2014)
Priority order: S14>T13>D10>C05>K04>P02.

APPENDIX D: THE SPIDERWEB NEBULA

We compare the H α intensity map with the UV surface brightness associated with the Spiderweb nebula to confirm if the extended H α distribution needs additional H α contributions from anything except star formation as examined by previous studies (e.g. Kurk et al. 2002; Nesvadba et al. 2006). We should note that these tentative analyses hold substantial error factors because of the filter flux loss and a lack of 3D spectral information. Fig. D1 shows the ratio map between H α-based SFR (SFR$_{H\alpha}$) and UV-inferred SFR (SFR$_{UV}$). We derive the SFRs via the Kennicutt (1998) prescription and both measurements do not include extinction correction. The flux photometry is based on the 1 arcsec^2 aperture photometry by the SExtractor instead of deriving fluxes in each pixel to increase the S/N levels. We derive observed H α flux from the narrow-band flux under the assumption that [N II]/ H α line ratio is 1 (Nesvadba et al. 2006). We estimate UV flux densities using the F814W image (λ_{rest} ~ 2500 Å at $z = 2.15$). PSF size of the F814W image is matched to those of narrow-band and K_s-band (FWHM = 0.63 arcsec). We use 2σ limiting magnitude (F814W = 27.28 mag in 1 arcsec^2 area) in faint regions.

Radial distributions of H α and UV -based SFRs are shown in Fig. D2. Each point corresponds to the aperture area centring on each pixel with a radial distance of 50 ph-kpc from the nucleus. To select diffuse H α nebula regions and remove the bright UV components around the Spiderweb galaxy, we simply mask the regions showing excesses of UV-inferred SFRs, as shown in Fig. D2. The figure thus only shows SFR$_{H\alpha}$ at which UV-luminous regions have been filtered. The lower panel shows the radial profile of the H α/UV ratio (SFR$_{H\alpha}$/SFR$_{UV}$) and corresponding dust-reddening values (E($B - V$)) needed to explain the excess of the ratio by assuming the Calzetti et al. (2000) extinction law. We also plot the roughly expected E($B - V$) suggested from the rest-UV colours between F475W and F814W assuming E($B - V$)$_{star}$ = E($B - V$)$_{nebula}$.
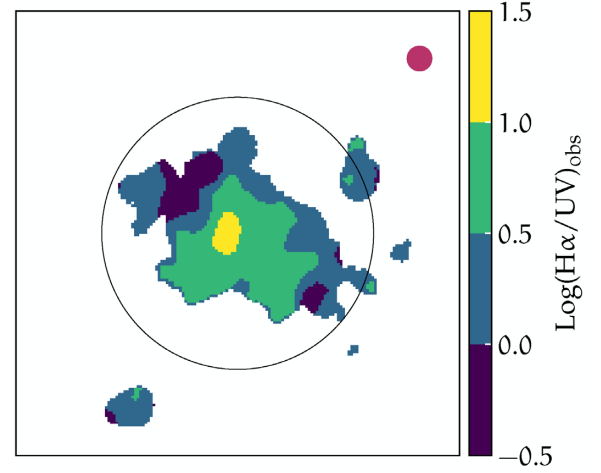
Figure D1. Observed H α/UV ratio map around the Spiderweb nebula. The colour bars on the right side show the observed log H α/UV ratio ($\equiv$log(SFR$_{H\alpha}$/SFR$_{UV}$)). The SFRs are derived based on 1 arcsec^2 area apertures as shown by the red circle. The figure only plots the regions with more than 2σ confidence levels in SB$_{H\alpha+[NII]}$. 1σ error of SB$_{H\alpha+[NII]}$ is 2.4×10^{41} erg s^{-1} arcsec^{-2} for a given aperture area. We replace faint regions at F814W by 2σ limiting magnitude (27.28 mag in 1 arcsec^2 area). The black open circle indicates 50 ph-kpc distance from the centre.
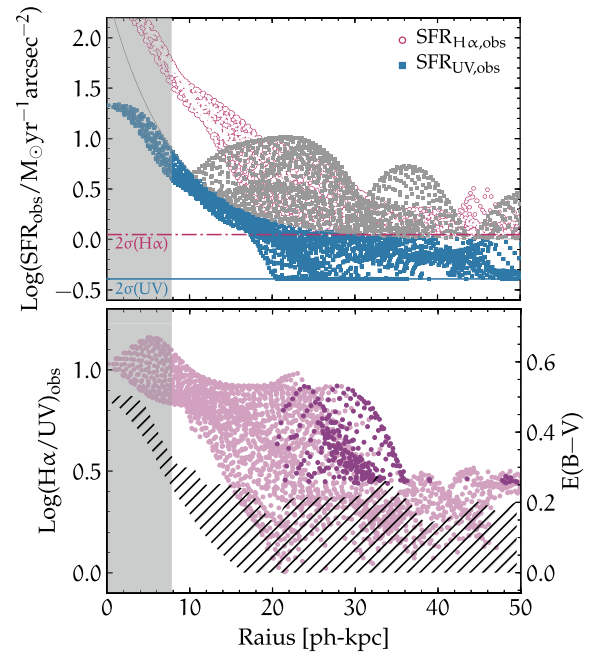
Figure D2. *Upper panel:* Radial profile of observed SFR$_{H\alpha, obs}$ (red open circles) and SFR$_{UV, obs}$ (blue filled squares). We mask the UV-excess regions as shown by grey squares. The red dash–dotted line and the blue solid lines indicate 2σ limits in SFR$_{H\alpha}$ and SFR$_{UV}$ respectively. *Lower panel:* The observed H α/UV ratio (purple circles). We employ 2σ limit mag in faint regions at F814W, which are highlighted by the darker colour. The black hatched areas show 95 percentile distribution of E($B-V$) suggested by F475W−F814W colours assuming the Calzetti et al. (2000) extinction law. The dust-reddening values correspond to the observed H α/UV ratio shown in the left axis when we assume E($B-V$)$_{star}$ = E($B-V$)$_{nebula}$ and dust-corrected SFR$_{H\alpha, corr}$ = SFR$_{UV, corr}$.

Since a substantial uncertainty of the dust correction around the nucleus is expected, we do not discuss the central position. On the other hand, when we consider that the outer diffuse UV and H α regions seem not to be heavily obscured as inferred from the $F475W - F814W$ colours, very high H α/UV ratios at the 10–30 ph-kpc radii cannot be examined only by the dust reddening. This strong excess may require an extra H α contribution from AGNs. These regions correspond to the south or west areas from the radio galaxy (Fig. D1) where no detectably bright UV components can be found (Fig. 12). Interestingly, these spots correspond to the location showing the high Ly α/ H α ratio (up to ∼7.6) and the radio jet (Kurk et al. 2002). Our results seem to support their findings, although more detailed analyses are required to resolve the energy sources.

This work does not compare in detail the radial distributions with those from other data sets such as the Ly α and the CO(1 − 0) images (Kurk et al. 2002; Emonts et al. 2016) since these spatial resolutions are too large to resolve these UV luminous components. Future deep high-resolution observation would allow a more detailed comparison and provide new insights into the physical origins of this extended multi-phase gas nebula.

This paper has been typeset from a TEX/LATEX file prepared by the author.